

The Broad-band Optical Properties of Galaxies with Redshifts $0.0 < z < 0.2$ ¹

Michael R. Blanton², David W. Hogg², Neta A. Bahcall³, Ivan K. Baldry⁴, J. Brinkmann⁵, István Csabai^{6,4}, Daniel Eisenstein⁷, Masataka Fukugita⁸, James E. Gunn³, Željko Ivezić³, D. Q. Lamb⁹, Robert H. Lupton³, Jon Loveday¹⁰, Jeffrey A. Munn¹¹, R. C. Nichol¹², Sadanori Okamura¹³, David J. Schlegel³, Kazuhiro Shimasaku¹³, Michael A. Strauss³, Michael S. Vogeley¹⁴ and David H. Weinberg¹⁵

ABSTRACT

Using photometry and spectroscopy of 144,609 galaxies from the Sloan Digital Sky Survey, we present bivariate distributions of pairs of seven galaxy properties: four optical colors, surface brightness, radial profile shape as measured by the Sérsic index, and absolute magnitude. In addition, we present the dependence of local galaxy density (smoothed on $8 h^{-1}$ Mpc scales) on all of these properties. Several classic, well-known relations among galaxy properties are evident at extremely high signal-to-noise ratio: the color–color relations of galaxies, the color–magnitude relations, the magnitude–surface brightness relation, and the dependence of density on color and absolute magnitude. We show that most of the i -band luminosity density in the universe is in the absolute magnitude and surface brightness ranges used: $-23.5 < M_{0.1i} < -17.0$ mag and $17 < \mu_{0.1i} < 24$ mag in 1 arcsec^2 (the notation ${}_b$ represents the b band shifted blueward by a factor $(1+z)$). Some of the relationships between parameters, in particular the color–magnitude relations, show stronger correlations for exponential galaxies and concentrated galaxies taken separately than for all galaxies taken together. We provide a simple set of fits of the dependence of galaxy properties on luminosity for these two sets of galaxies.

Subject headings: galaxies: fundamental parameters — galaxies: photometry — galaxies: statistics

¹Based on observations obtained with the Sloan Digital Sky Survey

² Center for Cosmology and Particle Physics, Department of Physics, New York University, 4 Washington Place, New York, NY 10003

³ Princeton University Observatory, Princeton, NJ 08544

⁴ Department of Physics and Astronomy, The Johns Hopkins University, Baltimore, MD 21218

⁵ Apache Point Observatory, 2001 Apache Point Road, P.O. Box 59, Sunspot, NM 88349-0059

⁶ Department of Physics, Eötvös University, Budapest, Pf. 32, Hungary, H-1518

⁷ Steward Observatory, 933 N. Cherry Ave., Tucson, AZ 85721

⁸ Institute for Cosmic Ray Research, University of Tokyo, Midori, Tanashi, Tokyo 188-8502, Japan

⁹ University of Chicago, Astronomy & Astrophysics Center, 5640 S. Ellis Ave., Chicago, IL 60637

¹⁰ Sussex Astronomy Centre, University of Sussex, Falmer, Brighton BN1 9QJ, UK

¹¹ U.S. Naval Observatory, 3450 Massachusetts Ave., NW, Washington, DC 20392-5420

¹² Department of Physics, Carnegie Mellon University, 5000 Forbes Avenue, Pittsburgh, PA 15213-3890

¹³ Department of Astronomy and Research Center for the Early Universe, School of Science, University of Tokyo, Tokyo 113-0033, Japan

¹⁴ Department of Physics, Drexel University, Philadelphia, PA 19104

¹⁵ Ohio State University, Department of Astronomy, Columbus, OH 43210

1. Motivation

There are strong correlations among the measurable physical properties of galaxies. The classification of galaxies along the visual morphological sequence described by Hubble (1936) correlates well with the dominance of their central bulge, their surface brightnesses, and their colors. These properties also correlate with other properties, such as metallicity, emission-line strength, luminosity in visual bands, neutral gas content, and the winding angle of the spiral structure (for a review, see Roberts & Haynes 1994). The surface brightnesses of giant galaxies classified morphologically as elliptical are known to be strongly correlated with their sizes (Kormendy 1977). Galaxy colors (at least of morphologically elliptical galaxies) are known to be strongly correlated with galaxy luminosity (Baum 1959; Faber 1973; Visvanathan & Sandage 1977; Terlevich et al. 2001). The gravitational mass of a galaxy is closely related to the luminosity and other galaxy properties. These galaxy relations manifest themselves in the Tully-Fisher relation for spiral galaxies (Tully & Fisher 1977; Burstein et al. 1997) and the Fundamental Plane for morphologically elliptical galaxies (Faber & Jackson 1976; Djorgovski & Davis 1987; Dressler et al. 1987; Burstein et al. 1997); Strauss & Willick (1995) review these dynamical relations. Furthermore, the environment of a galaxy is related to its type, in the sense that early-type galaxies are found in denser regions than late-type galaxies, as first noted by Hubble (1936) and as found by numerous subsequent investigators (Oemler 1974; Dressler 1980; Davis & Geller 1976; Giovanelli et al. 1986; Santiago & Strauss 1992; Guzzo et al. 1997; Hashimoto & Oemler 1999; Blanton 2000). In short, different physical properties of galaxies are closely related to each other.

In order to understand theoretically how galaxies formed and acquired their current properties, it is first necessary to characterize the observed distribution of galaxy properties in a comprehensive manner. Such a characterization is a primary goal of the Sloan Digital Sky Survey (SDSS; York et al. 2000). The SDSS has already created the largest sample to date (144,609 galaxies) of luminous galaxies with well-measured photometric and spectroscopic properties. As a first step in understanding the joint distribution of galaxy properties, we present here a study of the number density and luminosity density distributions of galaxy colors, profiles, luminosities, surface brightnesses, and local densities. Our purpose is to measure properties related to quantities that cosmological gasdynamical simulations (Nagamine et al. 2001; Pearce et al. 2001; Steinmetz & Navarro 2002) or semi-analytic models (Somerville et al. 2001; Mathis et al. 2002) can predict or will soon be able to predict, such as galaxy ages, sizes, stellar masses, and degrees of concentration.

The paper is organized as follows. Section 2 briefly describes the spectroscopic sample of the SDSS. Section 3 describes how we measure the set of properties studied here. Section 4 shows the number density and luminosity density distributions of these properties of galaxies, and provides simple fits for the dependence on luminosity of the properties of galaxies with nearly exponential radial profiles and those with more concentrated radial profiles. Section 7 summarizes and outlines future lines of research.

2. Data

2.1. Description of the Survey

The SDSS (York et al. 2000) is producing imaging and spectroscopic surveys over π steradians in the Northern Galactic Cap. A dedicated wide-field 2.5m telescope (Siegmund et al., in preparation) at Apache Point Observatory, Sunspot, New Mexico, images the sky in five bands between 3000 and 10000 Å (u , g , r , i , z ; Smith et al. 2002) using a drift-scanning, mosaic CCD camera (Gunn et al. 1998), detecting objects to a flux limit of $r \sim 22.5$ mags. The photometric quality of the observations are tracked using an automatic

photometricity monitor (Hogg et al. 2001). An automatic image-processing pipeline known as `photo` (Lupton et al. in preparation) processes the images and produces a catalog. The astrometric calibration is also performed by an automatic pipeline (Pier et al. 2002). One of the goals is to spectroscopically observe 900,000 galaxies, (down to $r_{\text{lim}} \approx 17.77$ mags), 100,000 Luminous Red Galaxies (Eisenstein et al. 2001), and 100,000 quasars (Fan 1999, Richards et al. 2002). This spectroscopic follow up uses two digital spectrographs on the same telescope as the imaging camera. Many of the details of the galaxy survey are described in the galaxy target selection paper (Strauss et al. 2002). Other aspects of the survey are described in the Early Data Release paper (EDR; Stoughton et al. 2002). The survey has begun in earnest, and to date has obtained about 30% of its intended data.

The SDSS images are reduced and catalogs are produced by the SDSS pipeline `photo`, which measures the sky background and the seeing conditions, and detects and measures objects. The photometry used here for the bulk of these objects was the same as that used when the objects were targeted. However, for those objects which were in the EDR photometric catalog, we used the better calibrations and photometry from the EDR. The versions of the SDSS pipeline `photo` used for the reductions of the data used here ranged from v5.0 to v5.2. The treatment of relatively small galaxies, which account for most of our sample, did not change substantially throughout these versions. The astrometric calibration is also performed by an automatic pipeline which obtains absolute positions to better than 0.1 arcsec (Pier et al. 2002).

The magnitudes are calibrated to a standard star network (Smith et al. 2002) approximately in the AB system. There are small differences between the system output by the SDSS pipelines and a true AB system, amounting to $\Delta m = -0.042, 0.036, 0.015, 0.013, -0.002$ in the $u, g, r, i,$ and z bands. Because these were discovered at a relatively late date in the preparation of this manuscript, we have not self-consistently included these shifts in our results (that is, by recalculating K -corrections based on the revised colors). Instead we have applied them *a posteriori* to our results in the $^{0.1}u, ^{0.1}g, ^{0.1}r, ^{0.1}i,$ and $^{0.1}z$ bands.

Object fluxes are determined several different ways by `photo`, as described in Stoughton et al. (2002). The primary measure of flux used for galaxies is the SDSS Petrosian magnitude, a modified version of the quantity proposed by Petrosian (1976). The essential feature of Petrosian magnitudes is that in the absence of seeing they measure a constant fraction of a galaxy’s light regardless of distance (or size). They are described in greater detail below (and also by Blanton et al. (2001) and Strauss et al. (2002)). As measures of the galaxy profile shape, `photo` also calculates the radius containing half the Petrosian flux (r_{50}) and that containing 90% of the Petrosian flux (r_{90}).

As described in Strauss et al. (2002), the bulk of the fibers in the SDSS are allocated to three samples: the Main Sample galaxies, the Luminous Red Galaxies, and quasars. Here we will concern ourselves solely with the Main Sample galaxies. There are three main criteria for their selection:

$$\begin{aligned} r_{\text{PSF}} - r_{\text{model}} &> s_{\text{limit}} \\ r_{\text{petro}} &< r_{\text{limit}}, \text{ and} \\ \mu_{50} &< \mu_{50,\text{limit}}. \end{aligned} \tag{1}$$

Here, r_{PSF} is an estimate of the magnitude using the local PSF as a weighted aperture, r_{model} is an estimate of the magnitude using the better of a de Vaucouleurs and an exponential fit to the image (accounting for seeing), r_{petro} is a modified form of the magnitude described by Petrosian (1976), and μ_{50} is the half-light surface brightness, defined as the average surface brightness within the radius which contains half of the Petrosian flux. All of these quantities are reddening-corrected using the dust maps of Schlegel et al. (1998). In practice, the values of the target selection parameters vary across the survey in a well-understood way, but for the bulk of the area, they are: $s_{\text{limit}} = 0.3$, $r_{\text{limit}} = 17.77$ mag, and $\mu_{50,\text{limit}} = 24.5$ mag in 1 arcsec².

Objects near the spectroscopic flux limit are nearly five magnitudes brighter than the photometric limit; that is, the fluxes are measured at signal-to-noise ratio of a few hundred.

Fibers are assigned to a set of circular tiles with a field of view 1.49 deg in radius by an automatic tiling pipeline (Blanton et al. 2002b). The targets are observed by a multi-fiber spectrograph capable of taking 640 spectra simultaneously (48 of the fibers are, in normal SDSS operations, devoted to sky fibers and spectrophotometric standards). An automatic data processing pipeline `spec2d` wavelength- and flux-calibrates the spectra and outputs a one-dimensional spectrum for each object (Schlegel, et al., in preparation). The resulting spectra have a resolution of $R \sim 2000$, cover roughly 3800 Å to 9000 Å, and typically have signal-to-noise per pixel around 10. This spectrum is then analyzed by another pipeline (`spectro1d`; SubbaRao, et al., in preparation) which classifies the spectrum and determines the redshift of the object. The redshifts used in the current analysis are determined independently using a separate pipeline originally designed specifically for bright stars (`specBS`; Schlegel, et al., in preparation) whose results are nearly identical for the main galaxy sample to the “official” SDSS redshift determination (over 99% of the objects obtain nearly identical redshifts in each pipeline).

As of April 2002, the SDSS had imaged and targeted 2,873 deg² of sky and taken spectra of approximately 350,000 objects over $\sim 2,000$ deg² of that area. The completeness over this area is roughly 91%; most of the missing galaxies (7% of the total) are lost due to the fact that two fibers on the same tile cannot be placed more closely than 55", about 1% are lost because they are not able to be assigned a fiber, and about 1% cannot have a redshift determined. From these data, we created a well-defined sample for calculating large-scale structure and galaxy property statistics, known as Large-Scale Structure `sample10`. `sample10` consists of all of the photometry for all of the targets over that area (as extracted from the internal SDSS operational database), all of the spectroscopic results (as output from `specBS`), and, most significantly, a description of the angular window function of the survey and the flux and surface brightness limits used for galaxies in each area of the sky. For most of the area, the same version of the analysis software used to create the target list was used in this sample. However, for the area covered by the Early Data Release (EDR; Stoughton et al. 2002) we used the version of the analysis software used for that data release, since it was substantially better than the early versions of the software used to target that area. For `photo`, the most important piece of analysis software run on the data, the versions used for the photometry range from `v5_0` to `v5_2`. The region covered by this sample is similar to, but not exactly, the region which will be released in the SDSS Data Release 1 (DR1), scheduled for January 1, 2003 (which will use `photo v5_3`, a newer version of the software which among other things improves the handling of large galaxies).

For the purposes of this paper, we further restrict `sample10` to galaxies in the redshift range $0.02 < z < 0.22$, the absolute magnitude range $-23.5 < M_{0.1i} < -17.0$ (assuming a Hubble constant $H_0 = 100h$ km⁻¹ s⁻¹ Mpc⁻¹ and $h = 1$), and to galaxies with $r > 14.5$. To calculate the distance modulus and the comoving volume we assume a model with $\Omega_0 = 0.3$ and $\Omega_\Lambda = 0.7$. These cuts restrict our sample to 144,609 galaxies. Figure 1 shows the distributions of *i*-band apparent magnitude (corrected for Galactic extinction) and Petrosian half-light radius for this sample of galaxies. The roll-off at the brightest and faintest magnitudes occurs because we have selected the sample in the *r*-band.

3. Galaxy Properties

Here we describe the set of galaxy properties whose joint distribution we intend to measure, and how those properties are measured by the SDSS. These properties are colors, luminosities, profile shapes, surface

brightnesses, and local densities.

3.1. Galaxy Colors and Luminosities

To measure the galaxy fluxes, we rely on the SDSS Petrosian magnitudes. The essential feature of Petrosian magnitudes is that in the absence of seeing they measure a constant fraction of a galaxy’s light regardless of distance (or size). More specifically, we define the “Petrosian ratio” \mathcal{R}_P at a radius r from the center of an object to be the ratio of the local surface brightness averaged over an annulus at r to the mean surface brightness within r :

$$\mathcal{R}_P(r) \equiv \frac{\int_{\alpha_{\text{lo}}r}^{\alpha_{\text{hi}}r} dr' 2\pi r' I(r') / [\pi(\alpha_{\text{hi}}^2 - \alpha_{\text{lo}}^2)r^2]}{\int_0^r dr' 2\pi r' I(r') / [\pi r^2]}, \quad (2)$$

where $I(r)$ is the azimuthally averaged surface brightness profile and $\alpha_{\text{lo}} < 1$, $\alpha_{\text{hi}} > 1$ define the annulus. The SDSS has adopted $\alpha_{\text{lo}} = 0.8$ and $\alpha_{\text{hi}} = 1.25$. The Petrosian radius r_P is the radius at which the \mathcal{R}_P falls below a threshold value $\mathcal{R}_{P,\text{lim}}$, set to 0.2 for the SDSS. The Petrosian flux is defined as the flux within a circular aperture with a radius equal to $N_P r_P$, where $N_P = 2$ for the SDSS. Petrosian magnitudes are described in greater detail by Blanton et al. (2001) and Strauss et al. (2002). While SDSS Petrosian magnitudes contain over 99% of the flux within an exponential profile, they contain only around 80% of the flux within a de Vaucouleurs profile in the absence of seeing; the fraction is higher in the presence of seeing, as shown by Blanton et al. (2001). For the SDSS, r_P is defined in the r -band and used to set the aperture for all the bands, such that the colors represent a measure of spectral energy distribution of the galaxy over a well-defined region of the galaxy.

Here we constrain the spectral energy distribution of the galaxies using the broad-band colors between the u , g , r , i , and z Petrosian magnitudes of the SDSS. A given set of observer-frame galaxy colors does not correspond uniquely to a particular SED, so we cannot infer with certainty the colors in any other frame. However, we can use our knowledge of the form of galaxy SEDs based on other data to make an attempt in order to interpolate between the observed-frame colors to a different frame by fitting a reasonable model SED to the galaxy colors. To do so, we use the routines in `kcorrect v1.11`, described by Blanton et al. (2002a), which uses a similar method to the method of Csabai et al. (2000) for calculating photometric redshifts. This method is demonstrably better than using the spectra (which suffer from the aperture biases associated with small-fiber spectroscopy, the inaccuracy of spectrophotometry, and the fact that we do not take spectra in the u and z bands; *cf.* Kochanek et al. 2000) and better than simply interpolating the magnitudes between bands (which does not account well for the 4000 Å break).

The essence of the method is that each set of observed magnitudes in the five bands is fit by a linear combination of four templates. The coefficients in the linear combination, and the templates themselves, are optimized to reproduce the observed magnitudes. For each galaxy, we now have a model for the SED. We use this SED to calculate the correction from the observed band to fixed frame bandpasses with shapes corresponding to the restframe coverage of galaxies at $z = 0.1$, the median redshift of the sample. The usual choice is to correct the colors to the $z = 0$ frame; however, this choice is not optimal, because most galaxies in our sample are not at $z = 0$. Figure 2 shows the responses of the unshifted SDSS and the SDSS system shifted to 0.1. We refer to bands in this system as ${}^{0.1}u$, ${}^{0.1}g$, ${}^{0.1}r$, ${}^{0.1}i$, and ${}^{0.1}z$, following the nomenclature of Blanton et al. (2002a). We note in passing that the K -correction for a galaxy *at* redshift $z = 0.1$ to this system is $-2.5 \log_{10}(1.1)$ for all bands independent of galaxy SED.

As a test of the validity of the colors, Figure 3 shows the distribution of galaxy colors as a function of redshift in a volume-limited sample in the range $-22.5 < M_{0.1i} < -21.5$ and $0.05 < z < 0.16$. The greyscale is the conditional distribution of color on redshift. The middle line in each panel is the median, the outer lines are the 10% and 90% quantiles. The distribution of galaxy colors is nearly constant with redshift, indicating that the K -corrections are relatively sensible. Note that we expect some change in these distributions given that galaxies evolve; in fact there is a hint of such evolution in the $^{0.1}u - g$ plot.

We use these estimated Petrosian $^{0.1}(u - g)$, $^{0.1}(g - r)$, $^{0.1}(r - i)$ and $^{0.1}(i - z)$ colors as our measures of the SED shape for each galaxy. As a measure of luminosity, we use the i -band flux converted to $^{0.1}i$ -band luminosity using the K -correction and the standard cosmological formulae for the distance modulus, assuming $\Omega_m = 0.3$ and $\Omega_\Lambda = 0.7$ (Hogg 1999).

3.2. Galaxy Profile Shape and Surface Brightness

One measure of the morphology of galaxies is the radial dependence of their surface brightness. For example, if one expresses this radial dependence in the form (suggested by Sérsic 1968):

$$I(r) = A \exp \left[-(r/r_0)^{1/n} \right], \quad (3)$$

galaxies with nearly exponential profiles (Sérsic index $n \sim 1$) tend to be considered “late-type,” while galaxies with nearly de Vaucouleurs profiles (Sérsic index $n \sim 4$) tend to be considered “early-type.” For this reason, we use measures of the azimuthally-averaged radial profiles of the galaxies in our analysis.

Although Strateva et al. (2001) and Shimasaku et al. (2001) have shown that the Petrosian inverse concentration index $1/c \equiv r_{50}/r_{90}$ is reasonably well correlated with eyeball morphological classifications for nearby, large galaxies, this parameter is too sensitive to the effects of seeing to be of great use for the bulk of the SDSS Main Sample. The top panel of Figure 4 shows the dependence of inverse concentration parameter on seeing for a volume-limited subsample, limited to galaxies with $-21 < M_{0.1i} < -20$ and $0.04 < z < 0.11$, demonstrating this dependence. This seeing dependence means that the same galaxy, observed under different conditions, can have considerably different measured concentrations. Even more importantly, it implies that the same galaxy, observed at different *distances*, will have different measured concentrations.

`photo` fits two-dimensional models to the galaxy images which account for the effects of seeing, but they are limited to the cases of $n = 1$ and $n = 4$, and in addition (because they were designed to study faint galaxy colors) for the versions of `photo` used here (before `v5.3`) they only performed the fit out to a relatively small radius compared to the size of an SDSS spectroscopic target galaxy. Thus, for our work here we have decided to fit the parameters in Equation (3) to the radial profile of each galaxy (accounting for the effects of seeing).

In order to do so, we find the parameters A , r_0 , and n in Equation (3) which minimize χ^2 with respect to the observed i -band radial profile and errors (as expressed by the `profMean` and `profErr` parameters in the SDSS catalog). When performing the fit, we convolve with the axisymmetric double Gaussian fit to the PSF determined by the SDSS photometric pipeline (Lupton et al., in preparation). The resulting distribution of χ^2 per degree of freedom peaks at approximately unity, but has a much larger tail than expected for gaussian errors; this suggests that a more detailed model (either for the seeing or for galaxy profiles) which better fits the data is possible to develop. After performing the fit, we can calculate the Petrosian inverse concentration parameter r_{50}/r_{90} based on the Sérsic index n . The top panel of Figure 4 shows this inverse concentration

parameter as a function of seeing for the volume-limited subsample. Our measure of galaxy profile shape is less seeing-dependent than the raw estimate r_{50}/r_{90} . We have fit Sérsic profiles to the profiles of all bands; the results of the g , r , i , and z profiles are all fairly consistent, while the u band results tend to be much less concentrated than the others.

It is worth examining how our axisymmetric Sérsic fit is affected by the non-axisymmetry of galaxies, and how it is related to other measures of profile shape, such as the Petrosian concentration parameter and the bulge-to-total (B/T) ratio. In the top panels of Figure 5, we investigate how our Sérsic fits behave for galaxies with Sérsic profiles and galaxies which consist of a de Vaucouleurs bulge plus an exponential disk. In each case we assume the galaxies are comparable in half-light radius to SDSS Main Sample galaxies. We use three different axis ratios b/a (as listed in Figure 5) by which we distort the galaxy image. We then project that image onto a grid of pixels of size $0.396''$, the size of SDSS pixels, apply single gaussian seeing with a standard deviation of $1.2''$, and then extract radial profiles using a similar scheme as used by SDSS `photo`. Using the single gaussian model for the seeing, we fit the Sérsic models to the resulting galaxy profiles. We perfectly reconstruct the case of b/a for the Sérsic profiles; for small axis ratios, we measure a higher concentration than we would for a circular image with the same profile as along the semi-major axis. For the bulge-plus-disk models, we find that the Sérsic index n is monotonically related to the B/T ratio of the bulge flux to the total flux.

The bottom panels of Figure 5 show the dependence of the Petrosian inverse concentration parameter r_{50}/r_{90} for galaxies of the same shapes as, but larger radii than, the galaxies in the top panels. This situation is meant to be similar to the conditions under which galaxies were observed by Shimasaku et al. (2001) and Strateva et al. (2001), who observed large, bright galaxies less affected by seeing than those in the SDSS Main sample. We find that r_{50}/r_{90} is closely related to Sérsic index and B/T .

We define the half-light surface brightness $r_{S,50}$ to be the average surface brightness within the Petrosian half-light radius for the Sérsic profile fit in the $^{0.1}i$ -band, in magnitudes in one arcsec², K -corrected and corrected for cosmological surface brightness dimming:

$$\mu_i \equiv m_{S,0.1i} + 2.5 \log_{10}(2\pi r_{S,50}^2) - 10 \log_{10}(1+z) - K_{0.1i}(z). \quad (4)$$

This measure of surface brightness is thus slightly different (in general, higher) than the raw estimate calculated from the Petrosian half-light radius output by the SDSS photometric pipeline, because it is corrected for seeing. Note that we have implicitly assumed that the K -correction of the observation of surface brightness remains unaffected by color gradients in the galaxy; because the K -correction from the observed i band to the $^{0.1}i$ band are expected to vary little with redshift and color (< 0.2 magnitudes) this approximation is not bad.

3.3. Local Galaxy Density

For each object in the sample we estimate the local galaxy density ρ as follows. First, we distribute a large number (2×10^6) of Poisson random points within the SDSS volume, distributed in redshift according to the selection function of the survey. The selection function is determined by an evolving $^{0.1}r$ -band Schechter function fit to the luminosity function of the following form (following Lin et al. 1999):

$$\Phi(L)dL = \phi_* \left(\frac{L}{L_*(z)} \right)^\alpha \exp(-L/L_*(z)), \quad (5)$$

where

$$L_*(z) = 10^{0.4Q(z-0.1)}L_*(z = 0.1). \quad (6)$$

Expressed in magnitudes, this implies $M_*(z) = M_*(z = 0.1) - Q(z - 0.1)$. If $Q > 0$, these formulae mean galaxies are brighter in the past. We indeed find that in order to explain the dependence of number counts on redshift in the survey, it is necessary to include the possibility that galaxy luminosities evolve. We perform this fit in the $^{0.1}r$ band and find the parameters:

$$\begin{aligned} \phi_* &= 3.22 \times 10^{-2} h^3 \text{ Mpc}^{-3}, \\ M_* &= -20.50, \\ \alpha &= -1.01, \\ Q &= 1.97. \end{aligned} \quad (7)$$

We do not give error bars for this fit, nor do we recommend this fit as our best estimate of the luminosity density or its evolution. We do not give error bars for this fit, nor do we recommend this fit as our best estimate of the luminosity density or its evolution. A more complete discussion of this topic is forthcoming in a separate paper. However, this fit is good enough to use to estimate local density. Using this fit, the magnitude limits as a function of position on the sky ($m_{r,\min}(\theta, \phi)$ and $m_{r,\max}(\theta, \phi)$), and the spectroscopic sampling fraction as a function of position on the sky ($f(\theta, \phi)$) we can calculate the selection function at any point on the sky.

Given the galaxy catalog and the random catalog, we count the number of galaxies N_g (including the galaxy in question) and the number of random points N_r in a $8 h^{-1}$ Mpc radius comoving sphere around each galaxy. We define

$$\rho \equiv \frac{N_g/\langle N_g \rangle}{N_r/\langle N_r \rangle}, \quad (8)$$

where $\langle N \rangle$ is the average expected number of objects in the sphere. We use this as an estimate of the local density relative to the mean. Because we use a spherical cell only 800 km s^{-1} in radius, this measure of density is affected somewhat by the velocity dispersions in the deep potential wells of clusters, in the sense that it will slightly underestimate the density in those regions. Also, since it is centered on a galaxy, and galaxies are clustered on these scales, its mean is greater than unity.

The local density is the only quantity considered here which is measured with a large amounts of noise for each object. The average “expected” number of objects for a Poisson distribution in each cell is about 14; the average actual number is about 37 (it is so much larger because the variance of the overdensity on this scales is around unity). This indicates that the average cell has errors of $\sim 20\%$. In particular, distant galaxies (which only have the brightest galaxies at that redshift within $8 h^{-1}$ Mpc) tend to have a measurement of ρ noisier than do close galaxies. One cannot really consider the joint distribution of the local density measured here and other galaxy properties, without accounting for the noise in the measure of the local density (Blanton 2000). Because of these effects, the galaxies which have the highest density estimates are just the galaxies with the smallest expected number of galaxies around them (and thus the highest expected noise in the measurement). Furthermore, the galaxies with the smallest expected number of galaxies around them are those at the highest redshift, and are therefore the highest luminosity galaxies. This introduces a correlation between the luminosity of a galaxy and the noise in our estimate of the density. The galaxies with the highest density estimates are high luminosity galaxies simply because of this artificial correlation between luminosity and measurement noise. This effect means that one cannot determine (from our measurements) the density dependence of luminosity (or any property correlated with it — that is, all galaxy properties).

Nevertheless, one can still meaningfully consider the median density within bins of other galaxy properties, because the increased noise for galaxies with higher mean distances does not affect the median density. As proof of this assertion, Figure 6 shows the density distribution as a function of redshift for several small ranges of absolute magnitude. The lines are the 10%, 50%, and 90% quantiles of the distribution. Although at large distances the distribution widens (the 10% and 90% quantiles decrease and increase, respectively), the median remains remarkably constant, indicating that it measures the density around galaxies consistently at high redshift and at low redshift. This consistency means that even when we divide galaxies into different groups which cover different redshift ranges (such as dividing by luminosity) we can make a fair comparison among the median local densities of the groups. This consistency happens to be the justification for the common practice of calculating the correlation function for galaxies of different luminosities, in different redshift ranges.

3.4. Contribution to Number Density

To compute the global number and luminosity densities, it is necessary to compute the number-density contribution $1/V_{\max}$ for each galaxy, where V_{\max} is the volume covered by the survey in which this galaxy could have been observed, accounting for the flux, surface brightness, and redshift limits as a function of angle (Schmidt 1968). This volume is calculated as follows:

$$V_{\max} = \frac{1}{4\pi} \int d\Omega f(\theta, \phi) \int_{z_{\min}(\theta, \phi)}^{z_{\max}(\theta, \phi)} dz \frac{dV}{dz}, \quad (9)$$

where $f(\theta, \phi)$ is described above and $z_{\min}(\theta, \phi)$ and $z_{\max}(\theta, \phi)$ are defined by:

$$\begin{aligned} z_{\min}(\theta, \phi) &= \max(z_{m,\min}(\theta, \phi), z_{\mu,\min}(\theta, \phi), 0.02) \\ z_{\max}(\theta, \phi) &= \min(z_{m,\max}(\theta, \phi), z_{\mu,\max}(\theta, \phi), 0.22). \end{aligned} \quad (10)$$

The flux limits $m_{r,\min}(\theta, \phi)$ (equal to 14.5 mag across the survey) and $m_{r,\max}(\theta, \phi)$ (approximately 17.77 mag) implicitly set $z_{m,\{\min\}}(\theta, \phi)$ by:

$$\begin{aligned} m_{r,\{\min\}}(\theta, \phi) &= M_{0.1r} + \text{DM}(z_{m,\{\min\}}(\theta, \phi)) \\ &+ K_{0.1r}(z_{m,\{\min\}}(\theta, \phi)). \end{aligned} \quad (11)$$

The surface brightness limits $\mu_{r,\min}(\theta, \phi)$ (in practice, too high surface brightness to matter for this sample) and $\mu_{r,\max}(\theta, \phi)$ (approximately 24.5 mag but variable in a known way across the survey) implicitly set $z_{\mu,\{\min\}}(\theta, \phi)$ by:

$$\begin{aligned} \mu_{r,\{\min\}}(\theta, \phi) &= \mu_{0.1r} + 10 \log_{10}(1 + z_{\mu,\{\min\}}(\theta, \phi)) \\ &+ K_{0.1r}(z_{\mu,\{\min\}}(\theta, \phi)). \end{aligned} \quad (12)$$

Note that we have implicitly assumed that the K -correction of the observation of surface brightness remains unaffected by color gradients in the galaxy. In practice, the surface brightness limits only rarely affect the V_{\max} determination.

The function $f(\theta, \phi)$ is the SDSS sampling fraction of galaxies as a function of position on the sky. The total sampling rate of galaxies is computed separately for each region covered by a unique set of spectroscopic survey tiles. We adopt the nomenclature of the 2dF (Percival et al. 2001): each such region is a “sector” (which corresponds identically to the “overlap regions” defined in Blanton et al. 2001). That is, in the case

of two overlapping tiles, the sampling is calculated separately in three sectors: the sector covered only by the first tile, the sector covered only by the second tile, and the sector covered by both. Each position on the sky is thereby assigned a sampling rate $f(\theta, \phi)$ equal to the number of redshifts of galaxy targets obtained in the region divided by the number of galaxy targets in the region. In regions covered by a single tile, typically $0.85 < f < 0.9$; in multiple plate regions, typically $f > 0.95$. These completenesses average to 0.92.

With V_{\max} , we calculate the global number and luminosity density contributions of any group of galaxies as $\sum_i 1/V_{i,\max}$ and $\sum_i L_i/V_{i,\max}$.

4. Results

4.1. Results for All Galaxies

4.1.1. Overview

Our primary results on the distributions of colors, surface brightnesses, profile shapes, luminosities and local densities of galaxies are shown in Figures 7–9. Each of these plots is a multi-panel figure showing some form of the bivariate distribution of every pair of galaxy properties in the off-diagonal plots. The plots on the diagonal show the univariate distribution of each quantity.

Figure 7 shows the projected number density distribution for all pairs of seven of our parameters, excluding density (for reasons described above). The V_{\max} values calculated above are used to calculate the contribution of each galaxy to the total number density. The panels above and below the diagonal are mirror images of each other. The grey scale is proportional to the square-root of the projected density in that plane. Contours in the plot represent loci of constant projected density enclosing 68% and 95% of the density. Figure 8 shows the bivariate $^{0.1}_i$ -band luminosity density distribution between all of our parameters. This figure is similar to Figure 7, only now each object contributes L/V_{\max} rather than $1/V_{\max}$ to the density.

Figure 9 shows the conditional number density distribution of all eight of our parameters relative to seven of them (only excluding density as an independent variable). That is, the greyscale represents the probability of a particular value of the quantity on the vertical axis, given the value of the quantity on the horizontal axis. This is equivalent to taking Figure 7, and for each vertical column of pixels renormalizing by the total density in that column. This plot is useful when the dependence of one quantity on another is strong in the regime where there are few galaxies (such as at high density or high luminosity). The histograms along the diagonal are the number density distributions of each quantity, and are identical to the histograms in Figure 7.

Some basic results are visible in these plots, which we review in the following subsections. Many of these results have been noted in the literature in the past. We will concentrate mostly on Figure 9, in which many of the relationships are easiest to see.

4.1.2. Dependence on Luminosity

The first simple result to point out from Figure 9 is the histogram in the right column and the second row from the top, which shows the luminosity function in the $^{0.1}_i$ -band. The function is close to a Schechter function, although because the vertical scale is linear, it may not appear familiar. Now consider the same

panel in Figure 8, which shows the luminosity density as a function of absolute magnitude. It is clear from this plot that the luminosity density is almost entirely contained within the range of absolute magnitudes shown ($-23.5 < M_{0.4} < -17.0$). We may further ask whether the surface brightness limits (around $\mu_{0.4} \sim 24.5$) greatly affect any estimate of the luminosity density from this sample. The histogram in Figure 8 showing the luminosity density as a function of surface brightness demonstrates that the luminosity density falls off long before the surface brightness limit becomes important. An even clearer demonstration of this fact is the panel showing the luminosity density versus $M_{0.4}$ and $\mu_{0.4}$. This panel shows that even at the lowest luminosities in the sample, the surface brightness limit excludes very little luminosity density. These results are in agreement with Blanton et al. (2001) (using early SDSS data) and Cross et al. (2001) (using early 2dFGRS data). A more careful analysis of the luminosity function and its evolution from this sample is being carried out by Blanton et al. (in preparation).

Next, let us follow the right column of Figure 9 down from the top. Each panel below the top panel shows the conditional dependence of a galaxy parameter on luminosity. These panels show many of the familiar relationships of galaxy properties to luminosity from previous observations. In sequence from top to bottom:

1. Local density is a strong function of luminosity. The most luminous galaxies exist preferentially in the densest regions of the universe. Density increases with luminosity for all absolute magnitudes above $M_{0.4} = -18$. At lower luminosities, the local density starts to increase again, which is potentially related to the existence of dwarf spheroidal galaxies in clusters. This result agrees with results from CfA (Hamilton 1988), the Optical Redshift Survey (hermit96a), as well as the recent results of Zehavi et al. (2002) in the SDSS and Norberg et al. (2002) in the 2dFGRS on the dependence of the correlation function amplitude on galaxy luminosity.
2. Highly luminous galaxies are more concentrated, and thus have higher Sérsic indices, than lower luminosity galaxies. This trend is consistent with high luminosity galaxies being preferentially “early-type.” However, even for the highest luminosity galaxies, the de Vaucouleurs profile ($n \sim 4$) is always more concentrated than more than 75% of the galaxies; the total number density of galaxies with $n > 3$ in our absolute magnitude range is $\sim 5\%$. Thus, either the number density fraction of “true ellipticals” is small in this absolute magnitude range or many “true ellipticals” are not de Vaucouleurs profile galaxies. That the Sérsic profile in most cases provides a better fit to the surface brightness profiles of morphologically-classified elliptical galaxies than the de Vaucouleurs profile has been shown previously by several groups (Prugniel & Simien 1997; Caon et al. 1993). We can try to compare to these results by dividing our sample by color. Figure 10 shows the dependence of n on absolute magnitude for three ranges of $^{0.1}(g-r)$. The Sérsic index n is clearly independent of luminosity for very blue galaxies (which are close to exponential). For very red galaxies the Sérsic index is a strong function of luminosity (paralleling the dependence of Sérsic index on luminosity found by Prugniel & Simien 1997 and Caon et al. 1993 for morphologically elliptical galaxies).
3. Luminosity and surface brightness are positively correlated at low luminosities, while at extremely high luminosity surface brightness declines with luminosity. As we will see below, this occurs because the surface brightnesses of highly concentrated galaxies, which tend to be highly luminous, decline with luminosity, while the surface brightnesses of exponential galaxies, which tend to be low luminosity, increase with luminosity. Note that constant size as a function of surface brightness would be a 45 degree line on the luminosity-surface brightness plot. At all luminosities, the surface brightness increases more slowly than luminosity, indicating that the median size of galaxies increases strongly with luminosity, especially for the most luminous galaxies.

4. The colors of galaxies depend strongly on luminosity, in the sense that more luminous galaxies are redder. The color-magnitude relation is most obvious in $^{0.1}(g-r)$, where separate red and blue populations are evident. This bimodality has also been noted in the observed $u-r$ colors by Strateva et al. (2001) and in the D4000 spectroscopic measurements of Kauffmann et al. (2002).

In short, there are strong dependencies of all parameters on luminosity.

4.1.3. Dependence on Profile Shape

The number density distribution of n , the Sérsic index, shows a strong peak at $n = 1$ in Figures 7 and 9, indicating that exponential galaxies are extremely common in the universe. Note that there is no peak in the number density at $n = 4$, which corresponds to a de Vaucouleurs profile, indicating that de Vaucouleurs galaxies lie along a continuum of galaxy concentration. Naturally, this result is subject to the limitations of our fit — which is based on an azimuthally averaged profile and uses a double gaussian approximation to the seeing. On the other hand, Figure 5 suggests that the effects of inclination are more likely to increase the observed Sérsic indices. To test the effects of inclination more empirically, we can restrict our sample to galaxies which are nearly face on (axis ratio greater than 0.8), according to the `photo` pipeline’s `ab_exp` and `ab_dev` measurements of the best fit axis ratios assuming an exponential or de Vaucouleurs model, respectively. Using either `ab_exp` or `ab_dev` as a measure of axis ratio does not lead the Sérsic fits to be closer to $n = 4$ or for any separate “concentrated” peak to appear in the distribution of Sérsic index n . Similarly, if we restrict our sample to galaxies which have χ^2 less than $N_d + \sqrt{N_d}$ (where N_d is the number of degrees of freedom in the fit), we also don’t find any peak at a de Vaucouleurs profile. The only subset of galaxies which we have found in our parameter space whose Sérsic index even close to “typically” $n = 4$ are very red ($^{0.1}(g-r) > 0.8$) and very luminous ($M_{0.1i} < -22.5$), which one can see in Figure 10; the actual number of such galaxies is very tiny. Thus, if there is a single parameter one can measure about galaxies which indicates whether it would be classified morphologically as an elliptical, and the typical such elliptical really has $n = 4$, that parameter is not any of those considered here.

The second column from the right in Figure 9 shows the dependence of each quantity on n , the Sérsic profile index. From top to bottom:

1. Local density does not depend on Sérsic index as much as it depends on luminosity, although exponential galaxies are in somewhat lower density regions than are concentrated galaxies (about 25% less overdense).
2. Galaxies with $n \approx 4$ have a luminosity function peaked at about $M_{0.1i} \approx -20.5$. The peak luminosity declines as the profile shape becomes closer and closer to exponential ($n = 1$), to the extent that it is clear that the peak of the luminosity function for pure exponential galaxies is well below our absolute magnitude limit of -17 . Due to these trends, the luminosity density distribution of n in Figure 8 is far flatter than the number density distribution, such that concentrated galaxies contribute a much larger fraction of the luminosity density than they do of the number density (for a more detailed analysis of this phenomenon, see Hogg et al. 2002).
3. The half-light surface brightnesses of exponential galaxies ($n \sim 1$) are distributed around $\mu_{0.1i} \sim 21$ while the surface brightnesses of concentrated galaxies are centered at much higher surface brightness ($\mu_{0.1i} \sim 19$).

4. The galaxies which are nearly exponential tend to be very blue in all colors ($^{0.1}(g-r) \sim 0.4$). For $n > 3$, galaxies are extremely homogeneous: constant and red colors, constant and high surface brightness, and constant average density.

4.1.4. Dependence on Surface Brightness

The third column from the right in Figure 9 shows the dependence of each quantity on $\mu_{0.1i}$;

1. Density is only a weak function of surface brightness on scales of $8 h^{-1}$ Mpc. Note that Zehavi et al. (2002) investigate the dependence of the correlation function on surface brightness; they find little dependence on these scales, but a strong dependence on smaller scales.
2. Paralleling the results for the Sérsic index, the luminosity function of high surface brightness objects is peaked at high luminosity, while at low surface brightness the luminosity function continues to increase until it passes our low luminosity limit. This result is similar to that found in SDSS commissioning data by Blanton et al. (2001) and in the 2dFGRS by Cross et al. (2001).
3. The profiles of high surface brightness galaxies are concentrated, while the profiles of most galaxies at lower surface brightness than $\mu_{0.1i} \sim 20$ are consistent with exponential.
4. The highest surface brightness objects are uniformly red, while fainter than $\mu_{0.1i} \sim 20$, surface brightness and color are positively correlated — the lower surface brightness a galaxy is, the bluer it tends to be.

4.1.5. Dependence on Color

The four left columns in Figures 7–9 show the relation between the four optical colors of galaxies and the other parameters. In Figure 7, two distinct peaks in the number density distribution are visible, most notably in the relation between $^{0.1}(u-g)$ and $^{0.1}(g-r)$. This result corresponds closely to the work of Strateva et al. (2001), which found a double peaked distribution of (observer-frame) $u-r$ color. The four left columns in Figure 9 show the dependence of all properties on the colors:

1. Density is a strong function of all colors. One expects this trend, based on the separate correlations of galaxy morphological classification with color (Roberts & Haynes 1994 and references therein) and environment (for example, Dressler 1980).
2. The luminosity function of galaxies which have $^{0.1}(g-r) \sim 1.0$ and $^{0.1}(r-i) \sim 0.45$ is peaked at high luminosity ($M_{0.1i} \sim -20.5$). The luminosity function of bluer galaxies increases right up to our lower luminosity limit. Redder than $^{0.1}(g-r) \sim 1.0$ or $^{0.1}(r-i) \sim 0.45$, the peak luminosity declines as well. This trend indicates that the reddest galaxies are a different population than those right around $^{0.1}(g-r) \sim 1.0$.
3. Blue galaxies have preferentially exponential profiles. The concentration of galaxy profiles is highest for galaxies with $^{0.1}(g-r) \sim 1.0$ or $^{0.1}(r-i) \sim 0.45$ (although, again, the median never reaches $n \sim 4$) and declines at redder colors again. Again, this trend suggests that the reddest galaxies are a special population; in particular, the fact that they tend to have profiles closer to exponential suggests that

they are edge-on spiral galaxies reddened by dust. This speculation is supported by the fact that the axial ratios measured by `photo` for these objects are low (~ 0.2 – 0.3).

4. The half-light surface brightness increases for redder galaxies, again until $^{0.1}(g-r) \sim 1.0$ or $^{0.1}(r-i) \sim 0.45$, at which point the surface brightness declines again. This trend may also be partly due to the fact that the reddest galaxies are probably dusty spirals; however, it is also due to the trend that at the higher luminosities, where galaxy colors are redder, galaxy half-light surface brightnesses tend to get lower with luminosity.

Furthermore, the colors are clearly highly correlated among themselves. In particular, measuring $^{0.1}(g-r)$ constrains the other colors to very small ranges.

4.2. Dividing Galaxies by Sérsic Index

We have so far explored only two-dimensional projections of an eight-dimensional space of parameters. It is interesting to explore a third dimension of this space. To do so, we divide the galaxies into two groups according to their Sérsic index. We choose an exponential group ($n < 1.5$) and a concentrated group ($n > 3$). (The results for the intermediate group look like a combination of the contributions from each group separately). Figures 11 and 12 show the conditional distribution of all our galaxy properties on all of the others for the exponential and concentrated groups, respectively. It is easy to identify which group of galaxies is considered from the panels involving the Sérsic index — for example, there is clearly no data for $n > 1.5$ in Figure 11.

The diagonal panels in each plot (which can be inferred from Figure 7) demonstrate that the Sérsic index does indeed divide galaxies into red, high surface brightness, luminous galaxies and blue, low surface brightness, underluminous galaxies. In particular, the luminosity function of the exponential group clearly is rising steeply through our low luminosity limit, while the luminosity function of the concentrated group is peaked at high luminosity.

Contrasting the conditional distributions of the exponential group in Figure 11 to those of the concentrated group in Figure 12 reveals that the properties of these populations have very different interrelationships. Most strikingly, the color-magnitude diagrams of these two classes separate extraordinarily well, into a tight red sequence (probably corresponding closely to the color-magnitude relation for morphologically elliptical galaxies Baum 1959) and a less tight, but undeniable, blue sequence.

Similarly, the dependence of surface brightness on luminosity differs markedly for the two classes. The surface brightness of exponential galaxies increases with luminosity (as does their size), while the surface brightness of concentrated galaxies decreases with their luminosity (while their size increases even more strongly). Another way of looking at the same issue is to consider the dependence of the physical half-light radius on absolute magnitude; Figure 13 shows this relationship for three ranges of Sérsic index n . Again, this figure shows that galaxy size closely correlates with luminosity, with a stronger dependence for de Vaucouleurs than for exponential galaxies. These results are comparable to those in Figure 44 of Bernardi et al. (2002); if one simply inverts the slope of the relationship between r_{50} and L (which yields a correct result if the relationship between the two is sufficiently linear and deterministic) we find $L_i \propto r_{i,50}^{-1.67}$, close to their result. These results also hold for the dependence of surface brightness on color; surface brightness correlates with color for exponential galaxies, but peaks at around $^{0.1}(g-r) \sim 1.0$ for concentrated galaxies. The results for concentrated galaxies are in good agreement with the work of Binggeli et al. (1984) (based

on morphologically elliptical galaxies).

Some of the most interesting results from these figures are the dependence of local density on galaxy properties for each type of galaxy profile taken separately. For example, the local density of exponential galaxies does not depend on surface brightness; for de Vaucouleurs, local density *decreases* slightly with surface brightness, a fact probably related to the decrease of luminosity with surface brightness for concentrated galaxies. It is only that higher surface brightness galaxies are more concentrated, and that concentrated galaxies are on average in higher density regions, that keeps the dependence of density on surface brightness flat for all galaxies.

The dependence of the local density on luminosity has a similar *shape* for concentrated galaxies and exponential galaxies, in the range of luminosities in which there is data for both types (less luminous than about $M_{0.4} \sim -22$). However, concentrated galaxies are naturally in slightly denser regions at any given luminosity. Meanwhile, for both concentrated and exponential galaxies, density depends strongly on color.

5. Fitting Median Properties as a Function of Luminosity

Figures 11 and 12 show that exponential and concentrated galaxies have colors, surface brightnesses, and local densities which are distinct from one another and which depend on galaxy luminosity. To quantify these relations, Figure 14 shows the $1/V_{\text{max}}$ -weighted median properties of both types as the boxes for exponential (thin lines) and concentrated (thick lines) galaxies (these lines are just the same as the median lines in Figures 11 and 12). The statistical uncertainties in the median containing 68% of the probability are shown as vertical lines (the width of the distribution is of course much larger).

We have fit these median relations in the following manner. First, we add a minimum variance in quadrature to the uncertainties on the points, which is $(0.02)^2$ for the colors and surface brightness, and is $(0.1)^2$ for density. We do so in order that our χ^2 minimization does not obsessively fit the few points with extremely tiny statistical uncertainties (who could easily be off by a small amount due to systematic errors in the data and our processing). Next, we fit a cubic polynomial to the resulting set of points and uncertainties. To be explicit, for property p we fit the function

$$p = p_0 + p_1(M_{0.4} + 21) + p_2(M_{0.4} + 21)^2 + p_3(M_{0.4} + 21)^3, \quad (13)$$

where $M_{0.4}$ is expressed in absolute magnitudes, the surface brightness is in magnitudes in 1 arcsec^2 , the colors are in magnitudes, and $\log_{10} \rho$ is unitless. We center the fit at $M_{0.4} = -21$ because that is near the center of our luminosity range. The resulting curves are shown in Figure 14 as continuous lines. They are all reasonable fits to the data over the range we have fit. The parameters p_i are listed in Table 1 for each property and galaxy profile type. We also list the standard deviations σ defined by the distribution of galaxies around the best fit curves, both in Figure 14 and in Table 1. However, as can be seen in Figures 11 and 12, gaussians of constant width are by no means adequate descriptions of the distributions around the median.

These relations may be useful for comparison to theory or to other observations. They allow one to predict the median properties of an exponential or concentrated galaxy given only the absolute magnitude. We caution that because there is significant scatter in all of these relations, one cannot reverse *these* fits to predict absolute magnitude from other galaxy properties.

6. Accessing the Two-dimensional Distribution Data

The two-dimensional projections of the number and luminosity density data used to create Figures 7, 8, 10, 11, 12, and 13 are available in FITS format from the electronic version of this article [**NOTE TO EDITOR: These electronic tables will be required; for now these can be found at <http://wassup.physics.nyu.edu/manyd/paper/>**].

The FITS file each have a single HDU containing three columns and one row. The first column contains M names (in string format) of the quantities listed in that file (corresponding to the x and y axes of the figures). The second column contains the ranges over those M quantities included in the figure (the first element of each range indicates the position of the left edge of the left-most pixel, and the second element of each range indicates the position of the right edge of the right-most pixel). The third column is a four dimensional array of dimensions (N, N, M, M) where M is the number of quantities, and N is the number of pixels on a side of each image. Each $N \times N$ subarray contains the data values used to create the greyscales in the corresponding figure of this paper. The values in the subarray are per unit “quantity m_1 ” per unit “quantity m_2 ”, where m_1 and m_2 represent the position in the (M, M) sized dimensions in the four dimensional array.

7. Conclusions and Future Work

In this paper, we have presented the number and luminosity density distributions of photometric galaxy properties as measured by the SDSS. Galaxy properties are highly correlated. Here are our main conclusions:

1. The most luminous galaxies comprise a homogeneous red, highly concentrated, high surface brightness population, and reside in locally dense regions. Underluminous galaxies are less homogeneous, but in general are bluer, less concentrated, lower surface brightness, and reside in less dense regions. These results are in qualitative agreement with previous work.
2. The relations among galaxy luminosities, surface brightnesses, and colors separate neatly once one has separated them into concentrated and unconcentrated (exponential) groups. Some of these relationships are well-known (such as the color–magnitude relation of concentrated galaxies; Baum 1959) while others are less commonly discussed (such as the color–magnitude relation for exponential galaxies).
3. Local density is a strong function of luminosity, at least for the most luminous galaxies, and on color for galaxies of all colors. This dependence of clustering on galaxy type has been quantified many times previously, early on in the work of Oemler (1974), later in the cluster studies of Dressler (1980), and also on larger scales by Davis & Geller (1976); Giovanelli et al. (1986); Santiago & Strauss (1992); Guzzo et al. (1997); Blanton (2000), and many others.

In addition, we make several more minor observations about the distribution of galaxy properties:

1. Optical galaxy colors all correlate very strongly with $^{0.1}(g-r)$ color. The distribution of $^{0.1}(g-r)$ is double-peaked.
2. Most of the luminosity density in the universe is contained in galaxies within our range of galaxy luminosities ($-23.5 < M_{0.4} < -17.0$).

3. The very reddest galaxies (which are small in number) are in optical colors exponential galaxies, not concentrated galaxies.
4. For all types of galaxies, size increases with luminosity. For concentrated galaxies, surface brightness decreases with luminosity for the most luminous galaxies. For exponential galaxies, surface brightness increases with luminosity.

Simple quantitative expressions of some of these results are contained in the parametric fits to the conditional distributions of Figure 14 and Table 1 as well as the two-dimensional projections given in the associated electronic tables. However, in future work we may characterize the distribution using a full seven-dimensional model of the distribution of properties.

A potentially important effect to account for in future analyses is the passive evolution of galaxy luminosities. Measurements of this evolution in the SDSS suggest that galaxy luminosities are brighter in the past (a trend of 4.2, 2.0, 1.6, 1.6, and 0.8 magnitudes per unit redshift in the $^{0.1}u$, $^{0.1}g$, $^{0.1}r$, $^{0.1}i$, and $^{0.1}z$ bands). While the difference in absolute magnitude over the whole redshift range is quite small (0.3 magnitudes) compared to the dynamic range in $^{0.1}i$ -band absolute magnitude, some of the colors may be affected significantly. Because the survey is flux limited, this effect can, in principle, alter the slope of our measurement of the color-magnitude relationship. For the trends quoted here, accounting for evolution would make the measured slope steeper, because the high luminosity galaxies are observed primarily at high redshift, and are observed to be bluer than they would be at the lower redshifts of the lower luminosity galaxies to which we are comparing them. For example, Bernardi et al. (2002) have found such evolution of the $g - r$ color-magnitude diagram in their early-type galaxy SDSS sample (their Figure 24). We note that one can detect the effect of not accounting for evolution by comparing the results of Blanton et al. (in preparation) for the evolution-corrected luminosity function at $z = 0.1$ to the $1/V_{\text{max}}$ -based estimate of the $^{0.1}i$ -band luminosity function presented here (our luminosity function extends to slightly higher luminosities than that estimate).

The scope of this paper has not allowed us to delve into a more detailed discussion of the individual relationships and their relation to galaxy formation theory. However, we could not do justice to these topics in the space and time available here, and leave this for the future, encouraging readers to use the data distributed here to perform similar work. We note that Kauffmann et al. (2002) have performed a similar analysis using fits to stellar population models. They also see bimodality in the distribution of galaxy properties, particular in their measure of the 4000 Å break. In addition, they find that because their estimated mass-to-light ratio (in their case in the $^{0.1}z$ -band) is a strong (and increasing) function of mass or luminosity, the dependence of surface mass density in a galaxy on total stellar mass is monotonic, even though the dependence of surface brightness on luminosity shows a maximum surface brightness at around an absolute magnitude of M_* . A particularly interesting application along these lines would be to consider the dependence of local density on stellar mass.

Two important photometric parameters missing from this space are color gradients and axis ratios. As it turns out, the color gradients of galaxies in our sample are usually quite small, partly because the central bulges of our spiral galaxies are blurred with the disks by seeing. Nevertheless, using a restricted sample of nearby galaxies, one can characterize this distribution. The distribution of axis ratios is related to the three-dimensional shape of the galaxy, so understanding the conditional distribution of this quantity on other parameters will yield a better understanding of galaxy geometry. Preliminary tests have shown that the axis ratios of our red, concentrated objects tend to be close to unity, whereas the axis ratios of blue, unconcentrated objects tend to differ significantly from unity, agreeing with the common understanding of

the nature of elliptical and spiral galaxies. Including a characterization of the two-dimensional shape of each galaxy would be an interesting way to expand the results found here.

We began this paper by noting that many galaxy properties have been known for decades to be correlated, and in particular to be correlated with position on the Hubble Sequence. Many readers will ask how galaxies of different morphological classifications are distributed in this space, a question we could address using a nearby subsample of the galaxies studied here. We have not done so here because we believe that morphological classification is not a sufficiently specified measurement to be straightforwardly interpreted. The position along the Hubble Sequence is determined by most galaxy classifiers from a consideration of a galaxy’s surface brightness, smoothness, concentration, axis ratio, the prominence of dust lanes, and spiral arm pitch angle. However, astronomy has not standardized the weights to be accorded by the classifier to each of these qualities of a galaxy image when placing each galaxy along the one-dimensional Hubble Sequence. In addition, the decision about a galaxy’s classification is highly dependent on the observing conditions, especially the distance of the galaxy from the observer, the dynamic range of the image, the passband of the observation, and the angle from which the galaxy is observed. Even when considering a single image and allowing only the classifier to vary, the repeatability of classification appears to be low ($\sigma \sim 2$ in units of Revised Hubble T type; Naim et al. 1995). Even this level of repeatability is not clearly due to the fact that classifiers all weight the various Hubble type criteria similarly, since the properties under consideration all correlate.

Nevertheless, as reviewed by Roberts & Haynes (1994), morphological classification is clearly important, since it does correlate with many physical properties of galaxies. Furthermore, we *can* specify certain aspects which determine morphological classification. For example, many investigators have quantified measures of surface brightness, concentration, smoothness/blobbiness (e.g. Naim et al. 1997), and lopsidedness (e.g. Rudnick et al. 2000), among others, and investigated the dependence of these measures on observing conditions. These efforts, of which this paper is a part, are forming a new approach to quantitative morphology that we hope will have a more direct and better specified connection to theoretical predictions.

MB and DWH acknowledge NASA NAG5-11669 for partial support. MB is grateful for the hospitality of the Department of Physics and Astronomy at the State University of New York at Stony Brook, who kindly provided computing facilities on his frequent visits there.

Funding for the creation and distribution of the SDSS has been provided by the Alfred P. Sloan Foundation, the Participating Institutions, the National Aeronautics and Space Administration, the National Science Foundation, the U.S. Department of Energy, the Japanese Monbukagakusho, and the Max Planck Society. The SDSS Web site is <http://www.sdss.org/>.

The SDSS is managed by the Astrophysical Research Consortium (ARC) for the Participating Institutions. The Participating Institutions are The University of Chicago, Fermilab, the Institute for Advanced Study, the Japan Participation Group, The Johns Hopkins University, Los Alamos National Laboratory, the Max-Planck-Institute for Astronomy (MPIA), the Max-Planck-Institute for Astrophysics (MPA), New Mexico State University, University of Pittsburgh, Princeton University, the United States Naval Observatory, and the University of Washington.

REFERENCES

Baum, W. A. 1959, PASP, 71, 106

- Bernardi, M. et al. 2002, AJ, submitted (astro-ph/0110344)
- Binggeli, B., Sandage, A., & Tarenghi, M. 1984, AJ, 89, 64
- Blanton, M. 2000, ApJ, 544, 63
- Blanton, M. R., Brinkmann, J., Csabai, I., Doi, M., Eisenstein, D. J., Fukugita, M., Gunn, J. E., Hogg, D. W., & Schlegel, D. J. 2002a, AJ, submitted (astro-ph/0205243)
- Blanton, M. R., Lin, H., Lupton, R. H., Maley, F. M., Young, N., Zehavi, I., & J., L. 2002b, AJ, submitted
- Blanton, M. R. et al. 2001, AJ, 121, 2358
- Bruzual A., G. & Charlot, S. 1993, ApJ, 405, 538
- Burstein, D., Bender, R., Faber, S., & Nolthenius, R. 1997, AJ, 114, 1365
- Caon, N., Capaccioli, M., & D’Onofrio, M. 1993, MNRAS, 265, 1013
- Cross, N. et al. 2001, MNRAS, 324, 825
- Csabai, I., Connolly, A. J., Szalay, A. S., & Budavári, T. 2000, AJ, 119, 69
- Davis, M. & Geller, M. J. 1976, ApJ, 208, 13
- Djorgovski, S. & Davis, M. 1987, ApJ, 313, 59
- Dressler, A. 1980, ApJ, 236, 351
- Dressler, A., Lynden-Bell, D., Burstein, D., Davies, R. L., Faber, S. M., Terlevich, R., & Wegner, G. 1987, ApJ, 313, 42
- Eisenstein, D. J. et al. 2001, accepted by AJ(astro-ph/0108153)
- Faber, S. M. 1973, ApJ, 179, 731
- Faber, S. M. & Jackson, R. E. 1976, ApJ, 204, 668
- Fan, X. 1999, AJ, 117, 2528
- Giovanelli, R., Haynes, M. P., & Chincarini, G. L. 1986, ApJ, 300, 77
- Gunn, J. E., Carr, M. A., Rockosi, C. M., Sekiguchi, M., et al. 1998, AJ, 116, 3040
- Guzzo, L., Strauss, M. A., Fisher, K. B., Giovanelli, R., & Haynes, M. P. 1997, ApJ, 489, 37
- Hamilton, A. J. S. 1988, ApJ, 331, L59
- Hashimoto, Y. & Oemler, A. J. 1999, ApJ, 510, 609
- Hogg, D. W. 1999, astro-ph/9905116
- Hogg, D. W., Blanton, M. R., Strateva, I., Bahcall, N. A., Brinkmann, J., Csabai, I., Doi, M., Fukugita, M., Hennessy, G., Ivezić, Z., Knapp, G. R., Lamb, D. Q., Lupton, R., Munn, J. A., Nichol, R., Schlegel, D. J., Schneider, D. P., & York, D. G. 2002, AJ, 124, 646
- Hogg, D. W., Finkbeiner, D. P., Schlegel, D. J., & Gunn, J. E. 2001, AJ, 122, 2129

- Hubble, E. P. 1936, *The Realm of the Nebulae* (New Haven: Yale University Press)
- Kauffmann, G., Heckman, T. M., White, S. D. M., Charlot, S., Tremonti, C., Peng, E. W., Seibert, M., Bernardi, M., Brinkmann, J., Castander, F., Csabai, I., Fukugita, M., Ivezić, Z., Munn, J., Nichol, R., Thakar, A., & Weinberg, D. 2002, submitted to MNRAS (astro-ph/0204055)
- Kochanek, C. S., Pahre, M. A., & Falco, E. E. 2000, submitted to ApJ (astro-ph/0011458)
- Kormendy, J. 1977, ApJ, 218, 333
- Lin, H., Yee, H. K. C., Carlberg, R. G., Morris, S. L., Sawicki, M., Patton, D. R., Wirth, G., & Shepherd, C. W. 1999, ApJ, 518, 533
- Mathis, H., Lemson, G., Springel, V., Kauffmann, G., White, S. D. M., Eldar, A., & Dekel, A. 2002, MNRAS, 333, 739
- Nagamine, K., Fukugita, M., Cen, R., & Ostriker, J. P. 2001, MNRAS, 327, L10
- Naim, A., Lahav, O., Buta, R. J., Corwin, H. G., de Vaucouleurs, G., Dressler, A., Huchra, J. P., van den Bergh, S., Raychaudhury, S., Sodre, L., & Storrie-Lombardi, M. C. 1995, MNRAS, 274, 1107
- Naim, A., Ratnatunga, K. U., & Griffiths, R. E. 1997, ApJS, 111, 357
- Norberg, P. et al. 2002, accepted by MNRAS (astro-ph/0111011)
- Oemler, A. 1974, ApJ, 194, 1
- Pearce, F. R., Jenkins, A., Frenk, C. S., White, S. D. M., Thomas, P. A., Couchman, H. M. P., Peacock, J. A., & Efstathiou, G. 2001, MNRAS, 326, 649
- Percival, W. J., Baugh, C. M., Bland-Hawthorn, J., Bridges, T., Cannon, R., Cole, S., Colless, M., Collins, C., Couch, W., Dalton, G., De Propris, R., Driver, S. P., Efstathiou, G., Ellis, R. S., Frenk, C. S., Glazebrook, K., Jackson, C., Lahav, O., Lewis, I., Lumsden, S., Maddox, S., Moody, S., Norberg, P., Peacock, J. A., Peterson, B. A., Sutherland, W., & Taylor, K. 2001, MNRAS, 327, 1297
- Petrosian, V. 1976, ApJ, 209, L1
- Pier, J. R., A., M. J., Hindsley, R. B., Hennessy, G. S., Kent, S. M., Lupton, R. H., & Ivezić, Z. 2002, submitted to AJ ??, ??
- Prugniel, P. & Simien, F. 1997, A&A, 321, 111
- Richards, G. et al. 2002, AJ, 123, 2945
- Roberts, M. S. & Haynes, M. P. 1994, ARA&A, 32, 115
- Rudnick, G., Rix, H., & Kennicutt, R. C. 2000, ApJ, 538, 569
- Santiago, B. X. & Strauss, M. A. 1992, ApJ, 387, 9
- Schlegel, D. J., Finkbeiner, D. P., & Davis, M. 1998, ApJ, 500, 525
- Sérsic, J. L. 1968, *Atlas de Galaxias Australes* (Cordoba: Obs. Astronomico)

- Shimasaku, K., Fukugita, M., Doi, M., Hamabe, M., Ichikawa, T., Okamura, S., Sekiguchi, M., Yasuda, N., Brinkmann, J., Csabai, I. ., Ichikawa, S., Ivezić, Z., Kunszt, P. Z., Schneider, D. P., Szokoly, G. P., Watanabe, M., & York, D. G. 2001, *AJ*, 122, 1238
- Smith, J. A., Tucker, D. L., Kent, S., Richmond, M. W., Fukugita, M., Ichikawa, T., Ichikawa, S.-I., Jorgensen, A. M., Uomoto, A., Gunn, J. E., Hamabe, M., Watanabe, M., Tolea, A., Henden, A., Annis, J., Pier, J. R., McKay, T. A., Brinkmann, J., Chen, B., Holtzman, J., Shimasaku, K., & York, D. G. 2002, *AJ*, 123, 2121
- Somerville, R. S., Lemson, G., Sigad, Y., Dekel, A., Kauffmann, G., & White, S. D. M. 2001, *MNRAS*, 320, 289
- Steinmetz, M. & Navarro, J. F. 2002, *New Astronomy*, 7, 155
- Stoughton, C. et al. 2002, *AJ*, 123, 485
- Strateva, I., Ivezić, Ž., Knapp, G. R., Narayanan, V. K., Strauss, M. A., Gunn, J. E., Lupton, R. H., Schlegel, D., Bahcall, N. A., Brinkmann, J., Brunner, R. J., Budavári, T. ., Csabai, I. ., Castander, F. J., Doi, M., Fukugita, M., Gyóry, Z., Hamabe, M., Hennessy, G., Ichikawa, T., Kunszt, P. Z., Lamb, D. Q., McKay, T. A., Okamura, S., Racusin, J., Sekiguchi, M., Schneider, D. P., Shimasaku, K., & York, D. 2001, *AJ*, 122, 1861
- Strauss, M. A. & Willick, J. 1995, *Phys. Rep.*, 261, 271
- Strauss, M. A. et al. 2002, *AJ*, accepted
- Terlevich, A. I., Caldwell, N., & Bower, R. G. 2001, *MNRAS*, 326, 1547
- Tully, R. B. & Fisher, J. R. 1977, *A&A*, 54, 661
- Visvanathan, N. & Sandage, A. 1977, *ApJ*, 216, 214
- York, D. et al. 2000, *AJ*, 120, 1579
- Zehavi, I. et al. 2002, *ApJ*, 571, 172

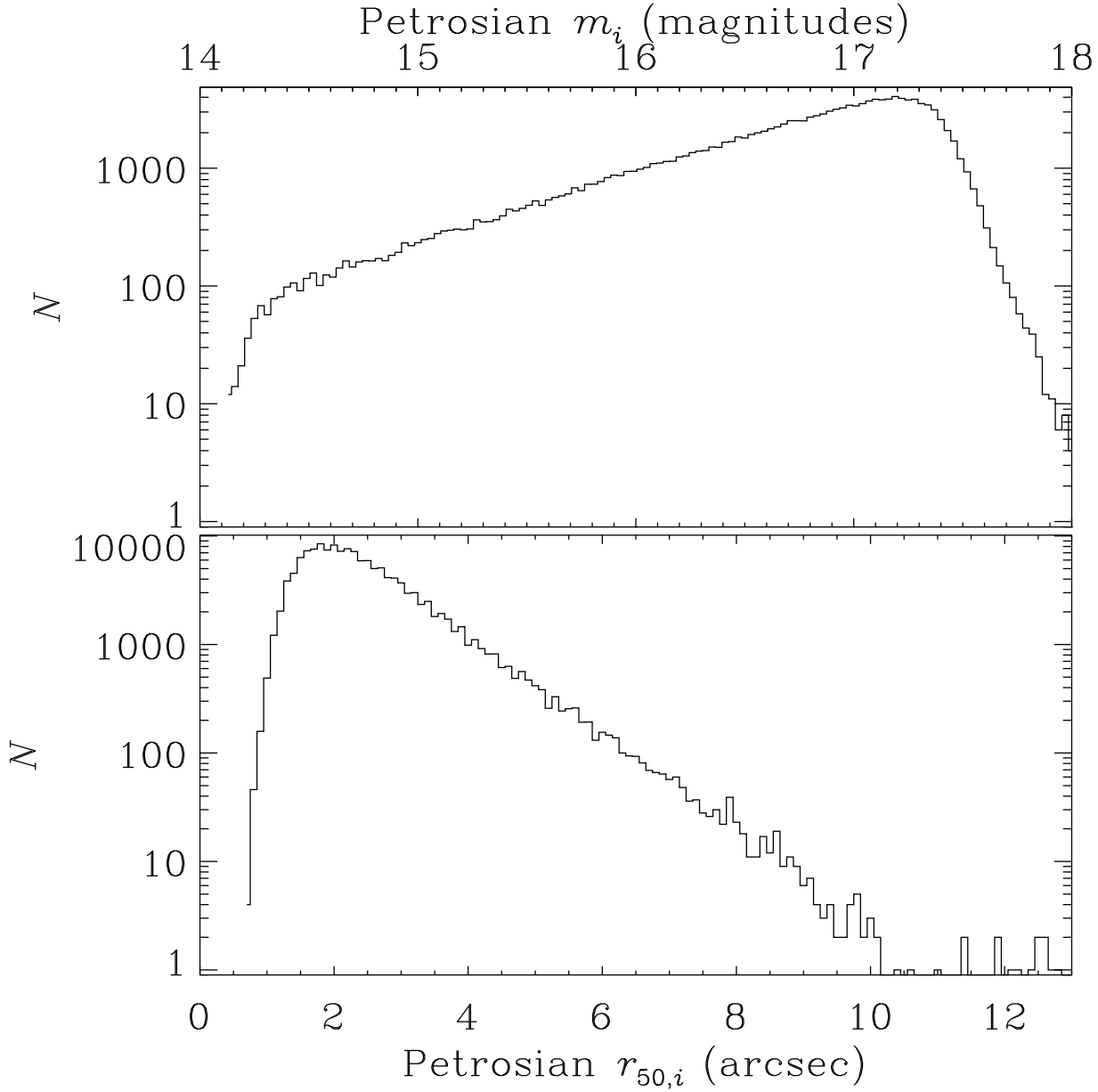


Fig. 1.— Distribution of reddening-corrected i -band Petrosian magnitude (top panel) and the observed i -band Petrosian half -light radius. The roll-offs at faint and bright magnitudes are due to the explicit conditions in our sample that $14.5 < r < 17.77$ (which are accounted for in our $1/V_{\text{max}}$ weighting).

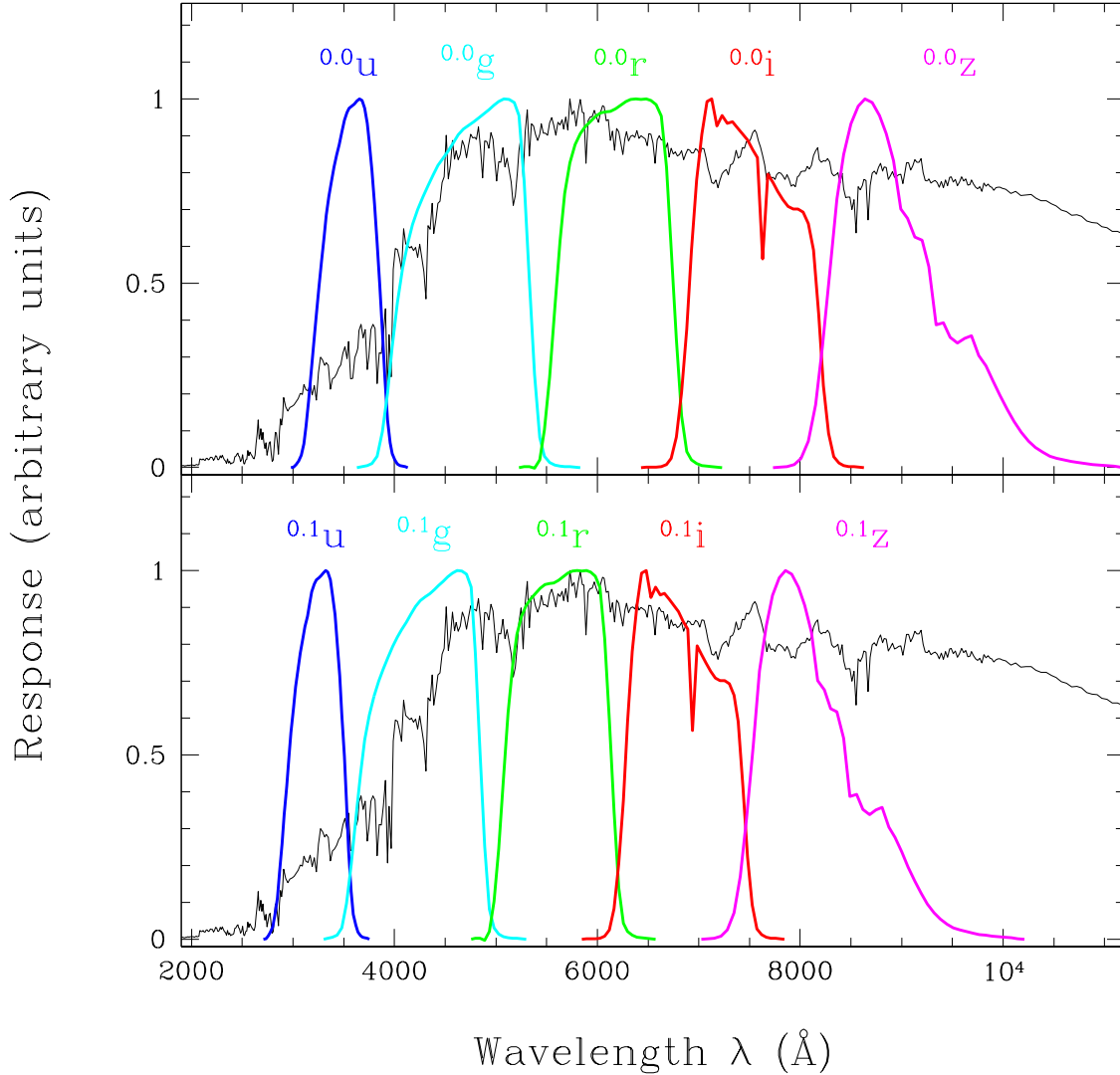


Fig. 2.— Demonstration of the differences between the unshifted SDSS filter system ($^{0.0}u$, $^{0.0}g$, $^{0.0}r$, $^{0.0}i$, $^{0.0}z$) in the top panel and the SDSS filter system shifted by 0.1 ($^{0.1}u$, $^{0.1}g$, $^{0.1}r$, $^{0.1}i$, $^{0.1}z$) in the bottom panel. Shown for comparison is a 4 Gyr-old instantaneous burst population from an update of the Bruzual A. & Charlot (1993) stellar population synthesis models. The K -corrections between the magnitudes of a galaxy in the unshifted SDSS system observed at redshift $z = 0.1$ and the magnitudes of that galaxy in the 0.1-shifted SDSS system observed at redshift $z = 0$ are independent of the galaxy’s spectral energy distribution (and for AB magnitudes are equal to $-2.5 \log_{10}(1 + 0.1)$ for all bands; Blanton et al. 2002a). This independence on spectral type makes the 0.1-shifted system a more appropriate system in which to express SDSS results, for which the median redshift is near redshift $z = 0.1$.

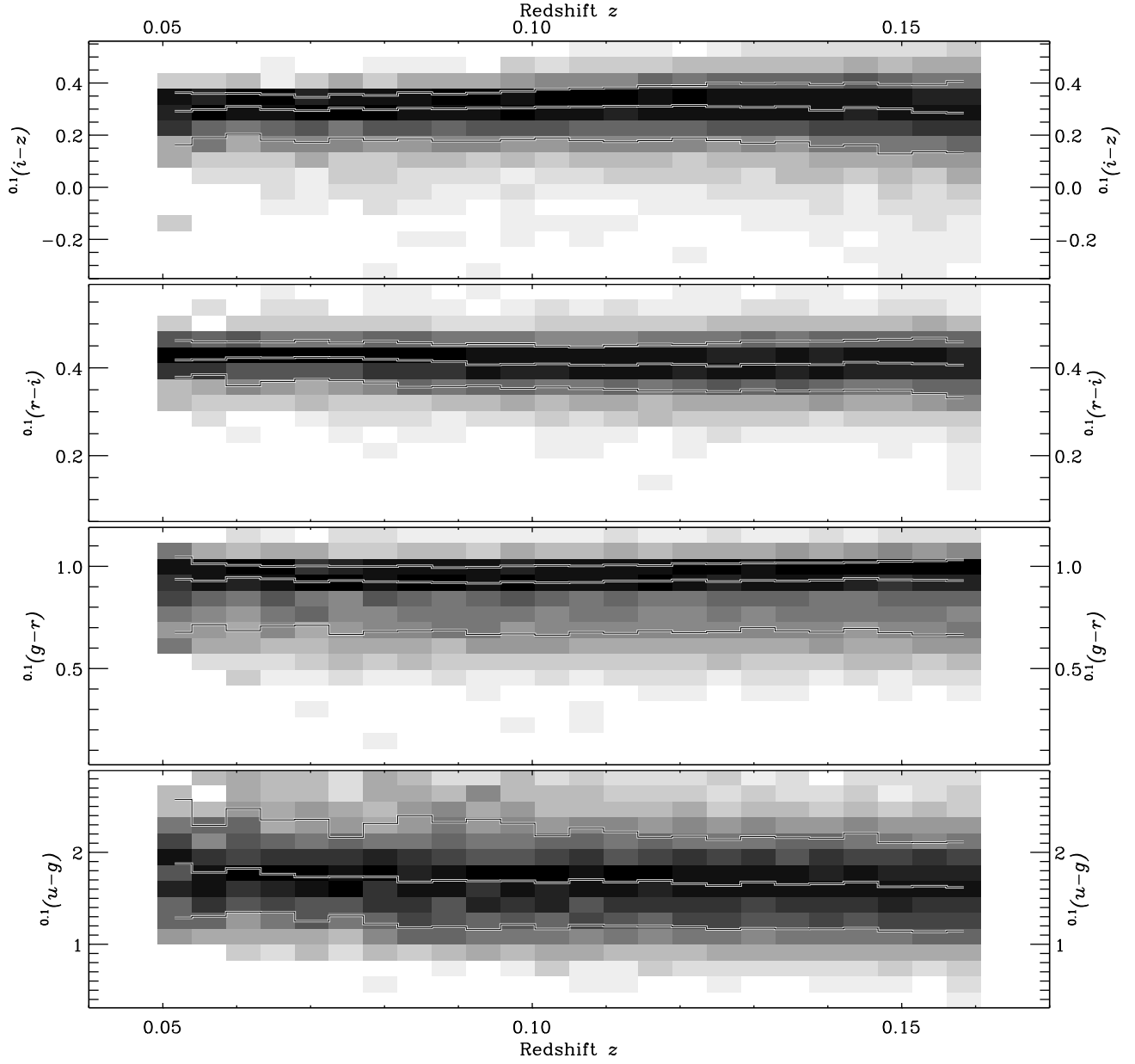


Fig. 3.— Distribution of fixed-frame colors at $z = 0.1$ as a function of redshift for a volume limited sample in the ranges $0.05 < z < 0.16$ and $-22.5 < M_{0.1r} < -21.5$. The greyscale is the conditional probability distribution of color on redshift, which is to say that each column is normalized separately. The lines indicate the 10%, 50% and 90% quantiles in each column. That the color distributions do not strongly evolve indicates that the K -corrections are reasonable. Some of the evolution apparent in the plot — for example the fact that the median $^{0.1}(u-g)$ color becomes bluer with cosmic time — may well reflect real galaxy evolution.

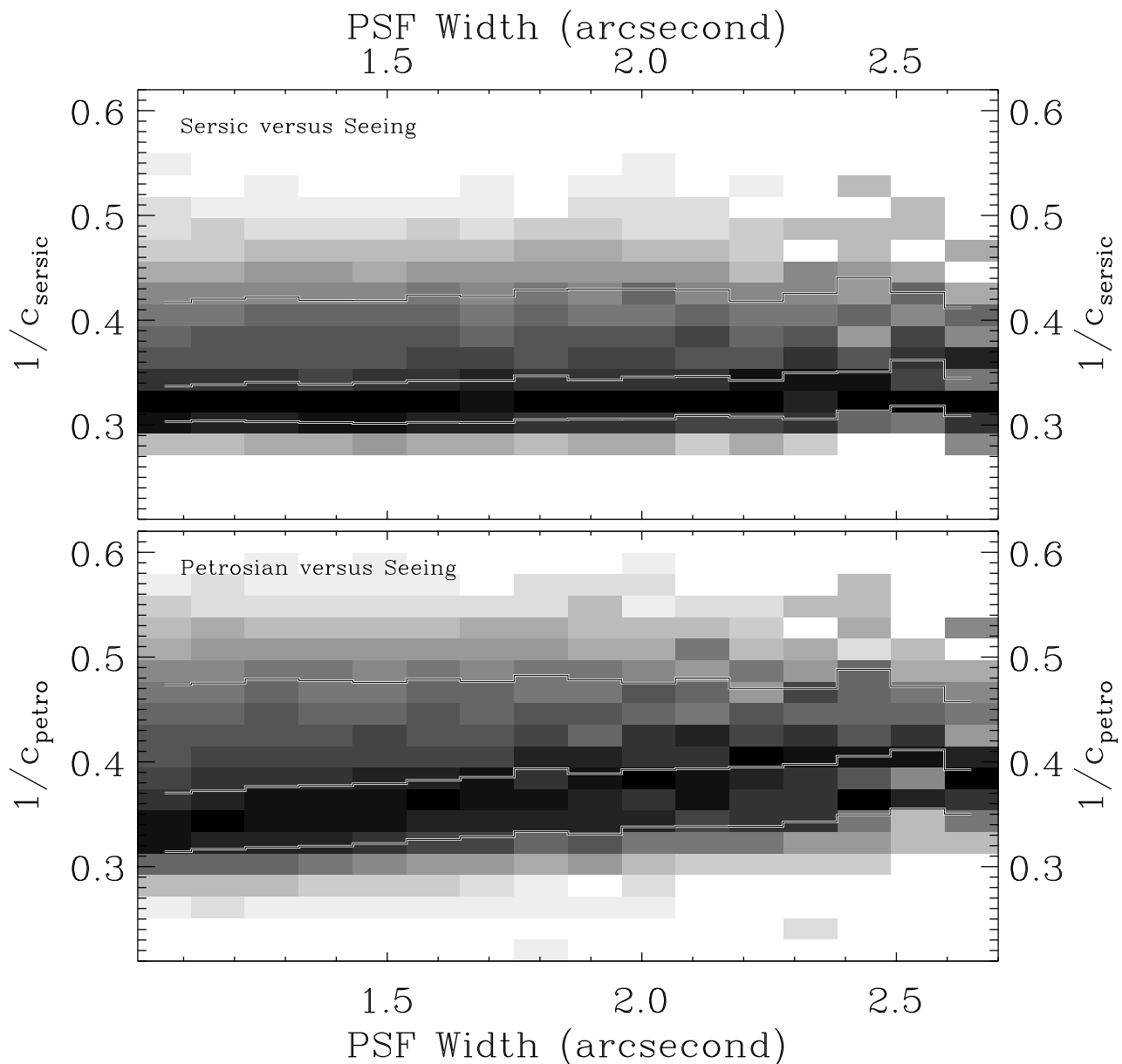


Fig. 4.— Dependence of the inverse concentration index on seeing for a volume limited sample in the ranges $0.04 < z < 0.11$ and $-21 < M_{0.4} < -20$. Each panel shows as a grey scale the conditional distribution of the $1/c \equiv r_{50}/r_{90}$ given the width of the seeing in arcseconds. (Because this is a conditional distribution, the greyscale does not indicate the amount of data which exists at a given seeing). As in Figure 3, the lines indicate the 10%, 50% and 90% quantiles in each column. The bottom panel shows the measured Petrosian $1/c$ as a function of seeing. There is a clear dependence of measured concentration on seeing; the median changes from around 0.37 to 0.42 from the best to worst seeing, respectively. Remember that any dependence on seeing also implies a dependence on apparent size, introducing a complicated interdependence of measured concentration with the actual concentration, the intrinsic size of the galaxy, the distance, and the seeing conditions. The top panel shows the Petrosian $1/c$ that would be measured from the Sérsic profile fit in the absence of seeing. This quantity shows almost no dependence on seeing conditions, indicating that this quantity eliminates, to some degree, the dependence of measured profile shape on observing conditions and galaxy size.

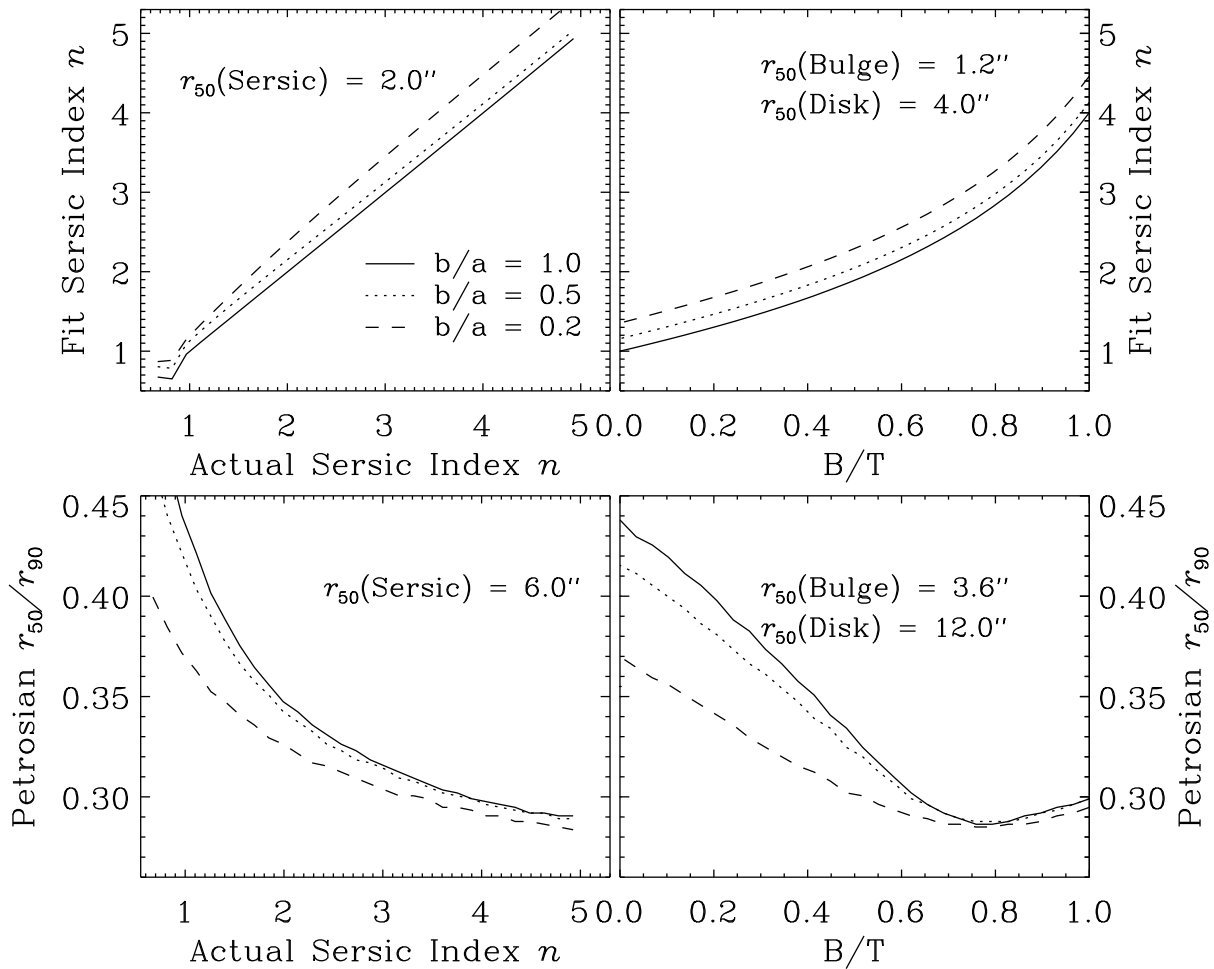


Fig. 5.— Brief exploration of the meaning of the Sérsic fits performed in this paper. We produced noiseless simulations of galaxies, pixelized using $0.396''$ pixels (the size of the SDSS pixels), and applied gaussian seeing with $\sigma = 1.2''$. We then extract radial profiles using the same annuli as used by the SDSS `photo` pipeline, and apply our Sérsic fit to the radial profile (equally weighting all points in the profile). In the left column we show the resulting index n in the fit; in the right column we show the Petrosian inverse concentration parameter $1/c = r_{50}/r_{90}$ for the this best-fit Sérsic profile (just for comparison). We choose two sorts of profiles: in the top panels, we show results for Sérsic profiles with various choices of Sérsic index n but a fixed r_{50} (as labeled); in the bottom panels, we show results for a bulge plus disk galaxy, with r_{50} for each component chosen as shown and a varying ratio B/T of total bulge flux to total disk flux. In both cases we choose three different axis ratios, assuming transparency. Deviations from axisymmetry under these conditions tends to increase the concentration of the galaxy; on the other hand, one might expect different behavior for opaque objects.

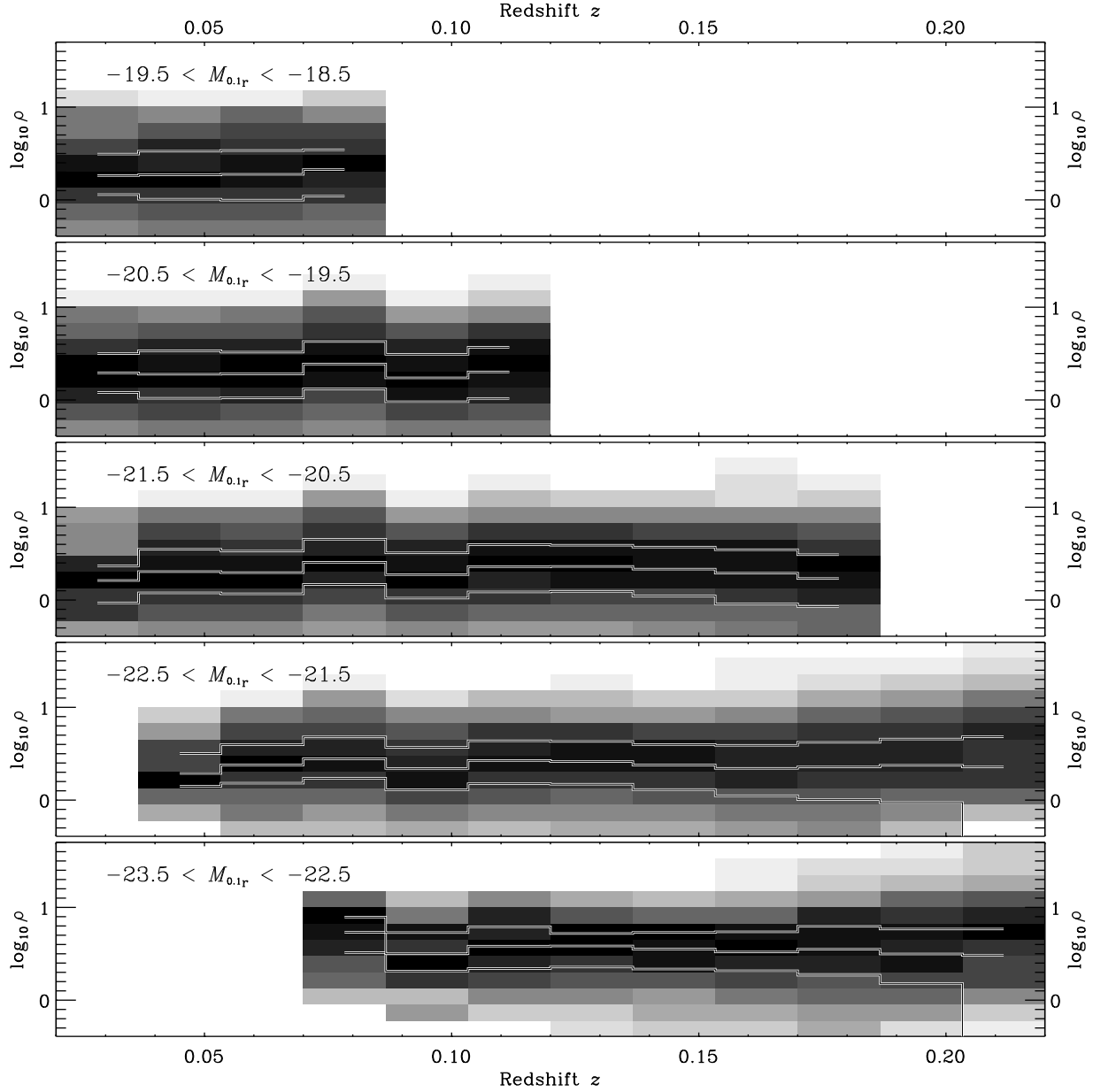


Fig. 6.— Estimate of the local density within $8 h^{-1}$ Mpc as a function of redshift, for a series of volume limited samples with the absolute magnitude limits shown. As in Figure 3, the greyscale is the conditional distribution of the local density given the redshift, and the lines are the 10%, 50% and 90% quantiles. The dependence of clustering on luminosity is evident. The impact of Poisson noise on the local density estimates becomes noticeable as the sample approaches $z \approx 0.2$, as the distribution widens. However, the median local density appears nearly constant, indicating that it is a reliable estimator of local density.

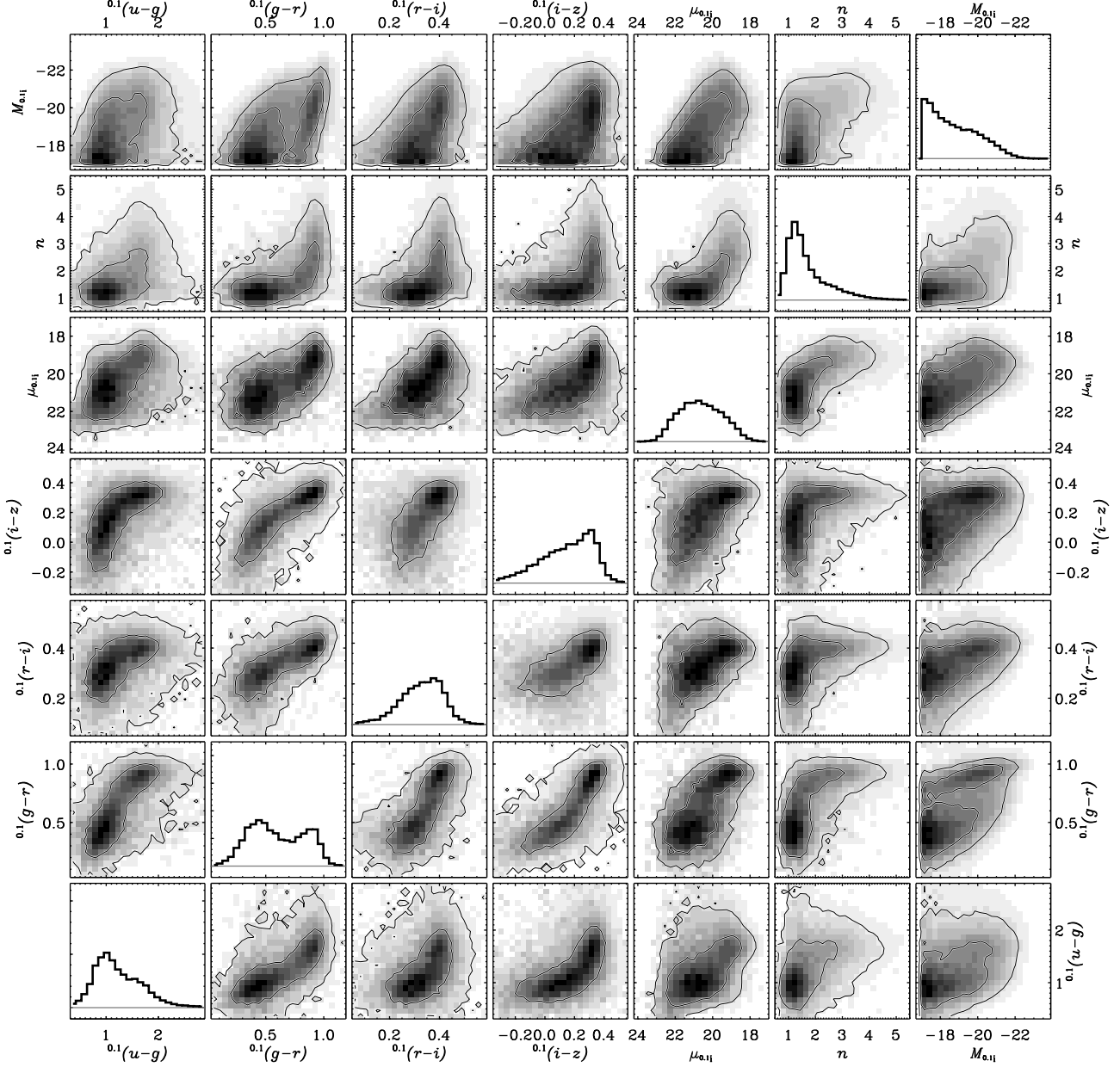


Fig. 7.— Projection of the number density of galaxies in our seven-dimensional space onto each pair of dimensions. All images have a square-root stretch applied to increase the dynamic range of the plot. Contours indicate the regions containing 68% and 95% of the total number density of galaxies in this sample. The upper and low triangles are identical mirror images. The histograms along the diagonal show the distribution of galaxies in each dimension.

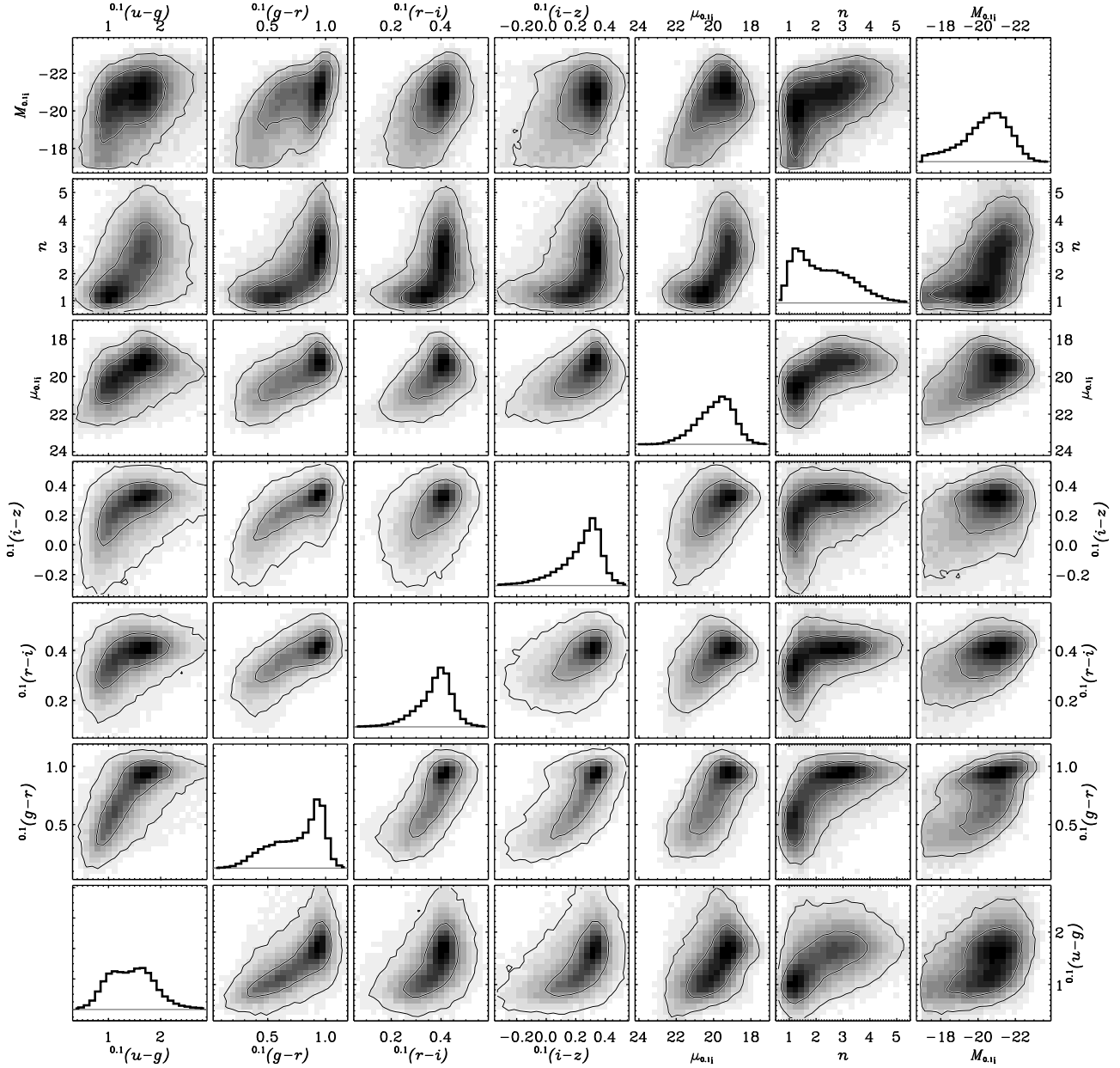


Fig. 8.— Same as Figure 7, but plotting luminosity density rather than number density. It is clear from these plots that the luminosity density contribution from galaxies below the absolute magnitude and surface brightness limits of this sample is small.

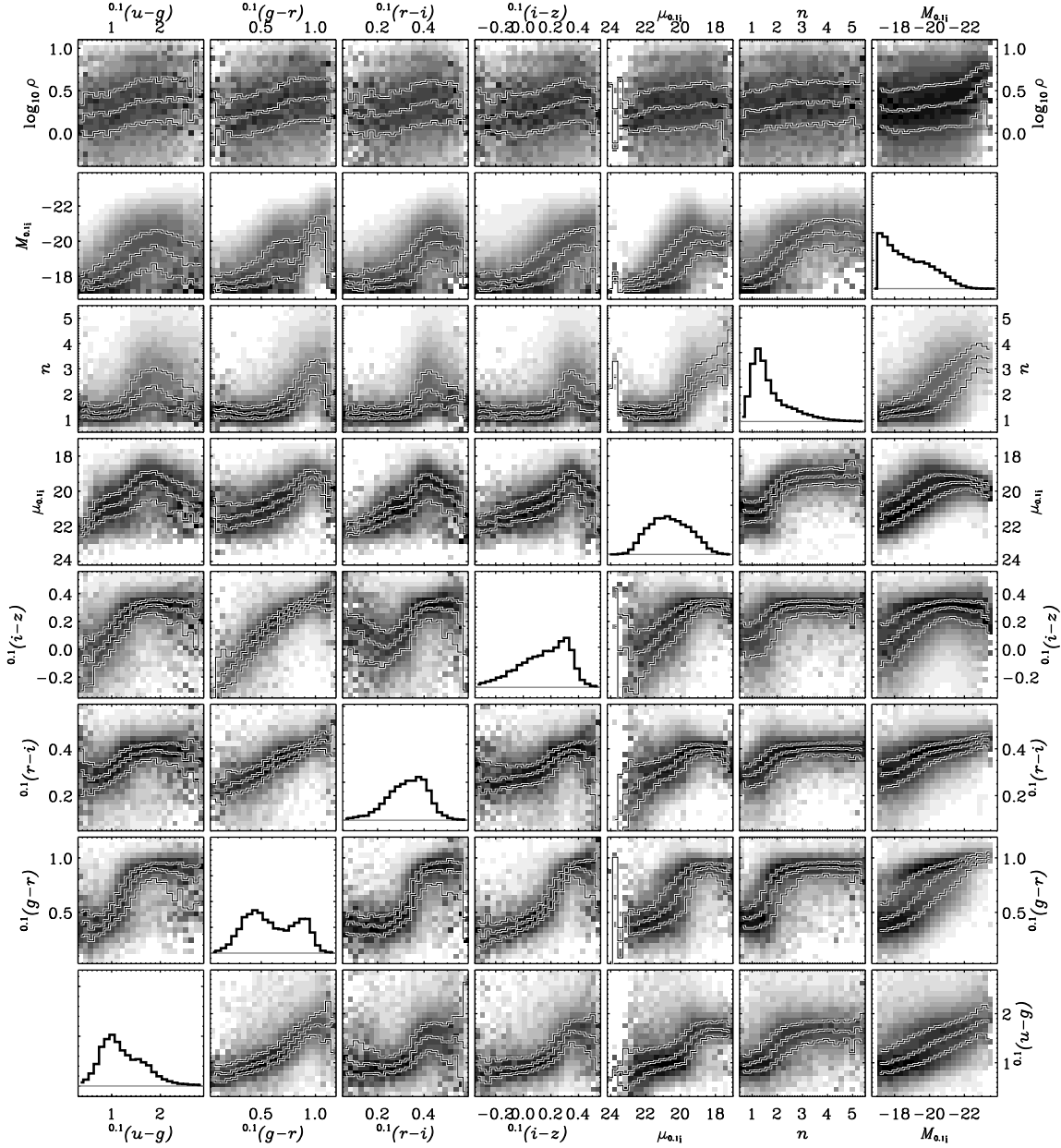


Fig. 9.— Similar to Figure 7, but showing the conditional distribution of each quantity on the vertical axis with respect to the quantity on the horizontal axis. Thus, the upper left panel shows the conditional distribution $P(\log_{10} \rho | M_{0.1i})$ while the lower right panel shows the conditional distribution $P(^{0.1}(u-g) | M_{0.1i})$. In other words, these plots are equivalent to normalizing separately each column of each panel in Figure 7. The lines shown are quartiles of the conditional number density distribution. While we left out local density in Figures 7 and 8 because it is a noisy quantity and to calculate its distribution requires accounting for this noise, we include it here since (as concluded in the text) it is reasonable to look at the dependence of the median local density on other galaxy properties.

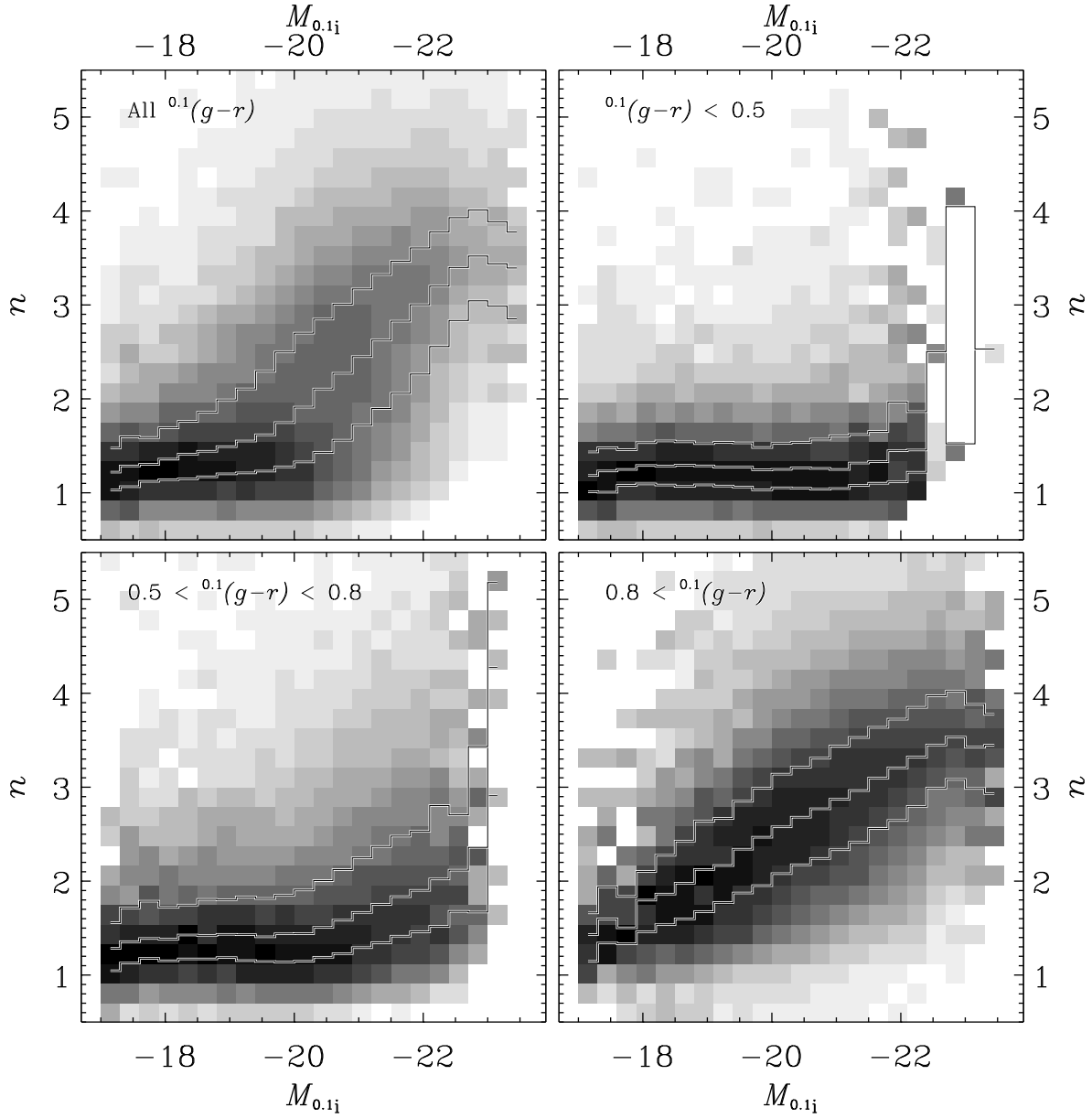


Fig. 10.— Similar to Figure 9, but restricting only to the dependence of Sérsic index n on absolute magnitude, for several ranges of $^{0.1}(g-r)$ color, as labeled. Blue galaxies are overwhelmingly exponential; red galaxies become more and more concentrated as they become more luminous.

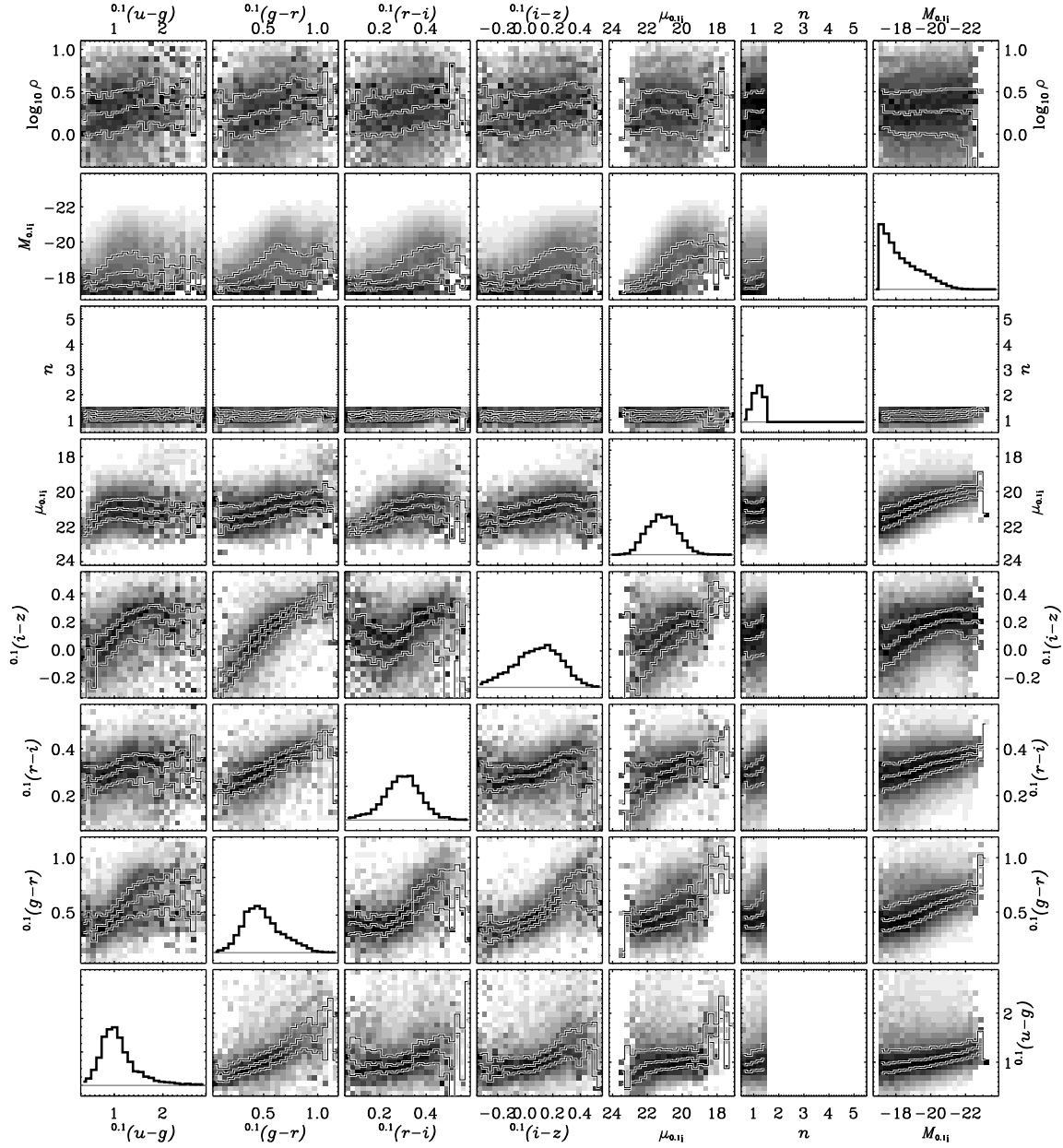


Fig. 11.— Similar to Figure 9, but only including galaxies with $n < 1.5$ (the exponential galaxies).

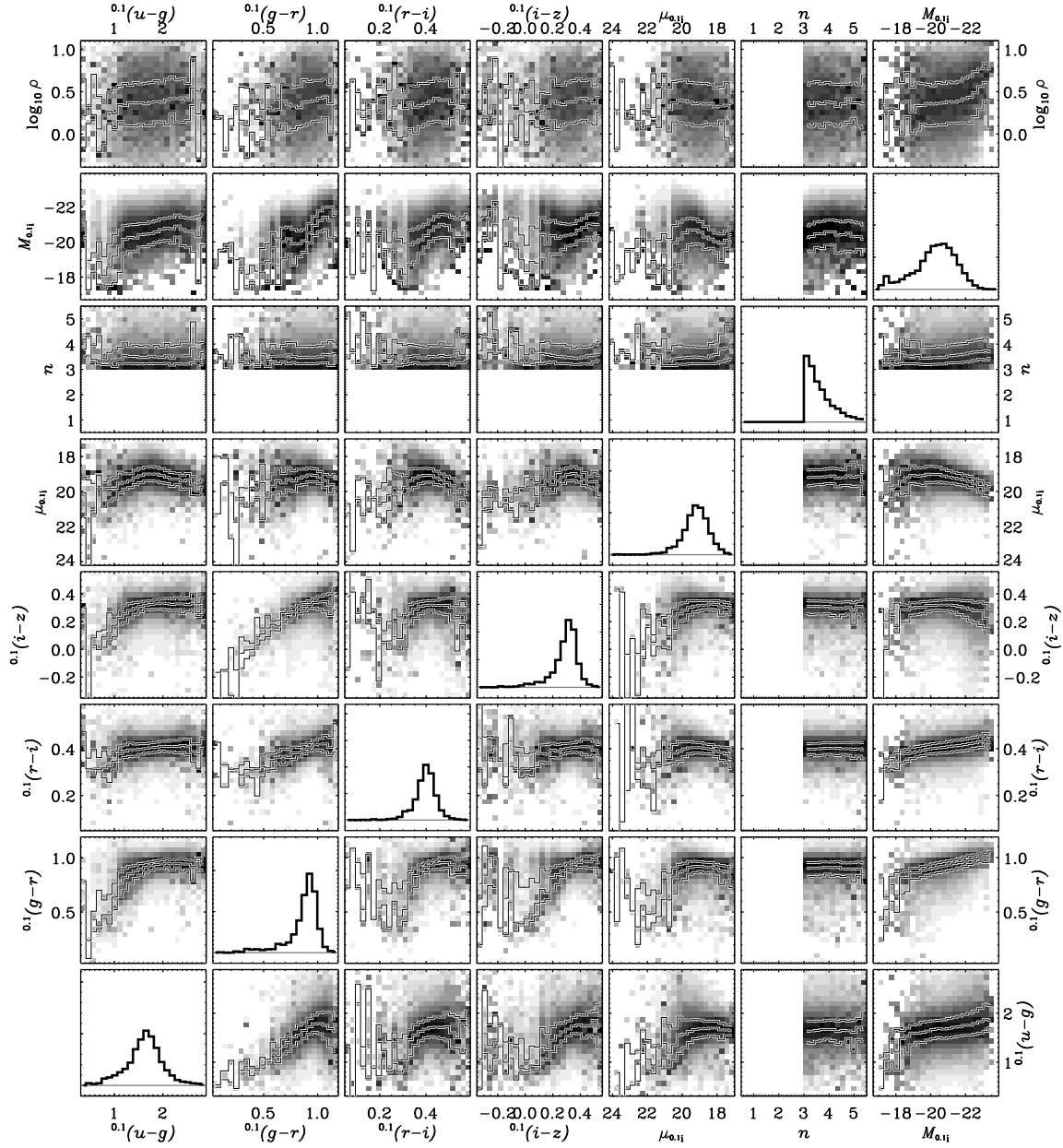


Fig. 12.— Similar to Figure 9, but only including galaxies with $n > 3.0$ (the concentrated galaxies).

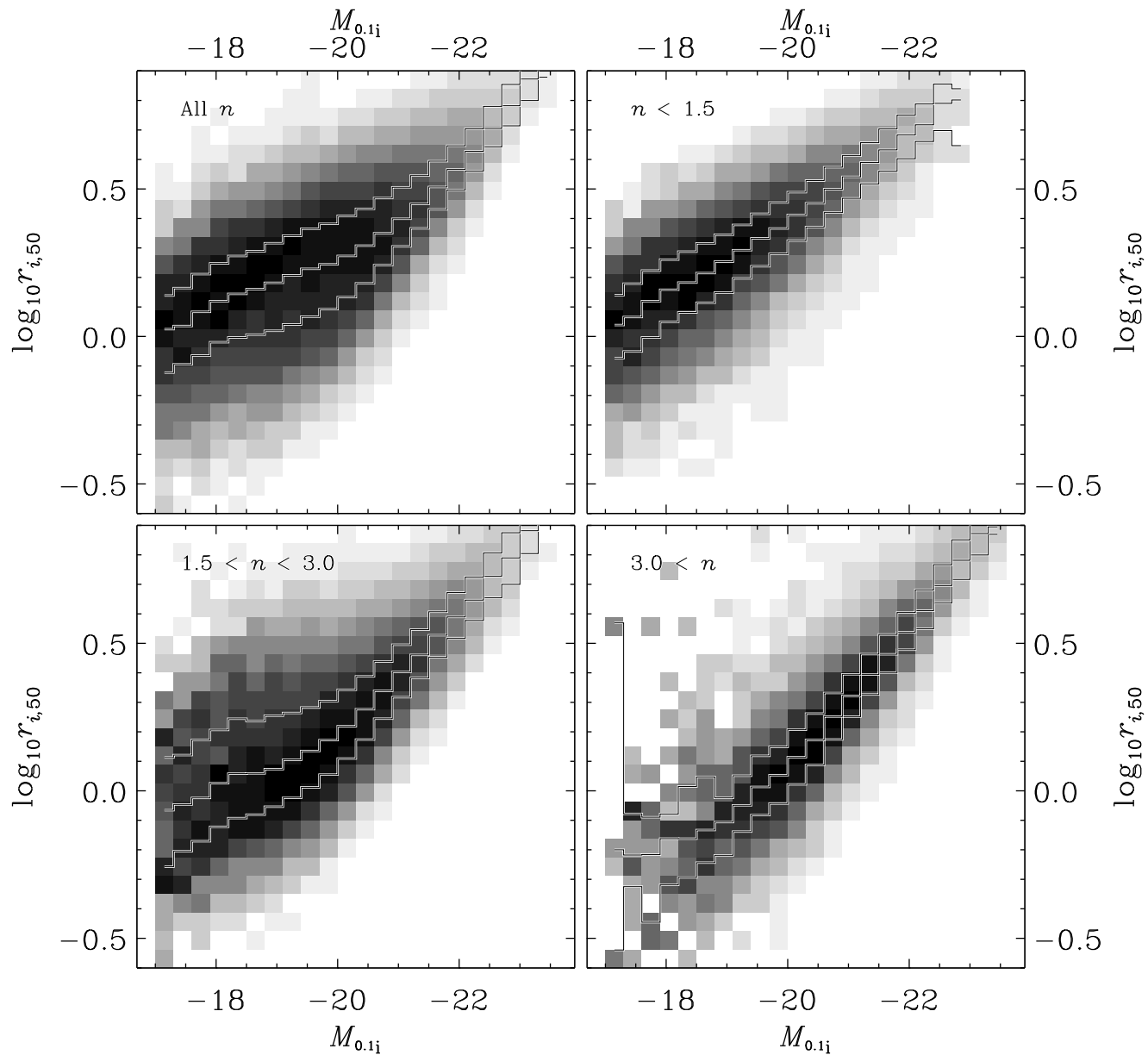


Fig. 13.— Similar to Figure 10, only showing the distribution of the Sérsic half-light radius r_{50} (in units of h^{-1} kpc) as a function of absolute magnitude for several ranges of Sérsic index. The results here are simply another expression of the relationship between absolute magnitude and half-light surface brightness shown in Figures 9, 11, and 12.

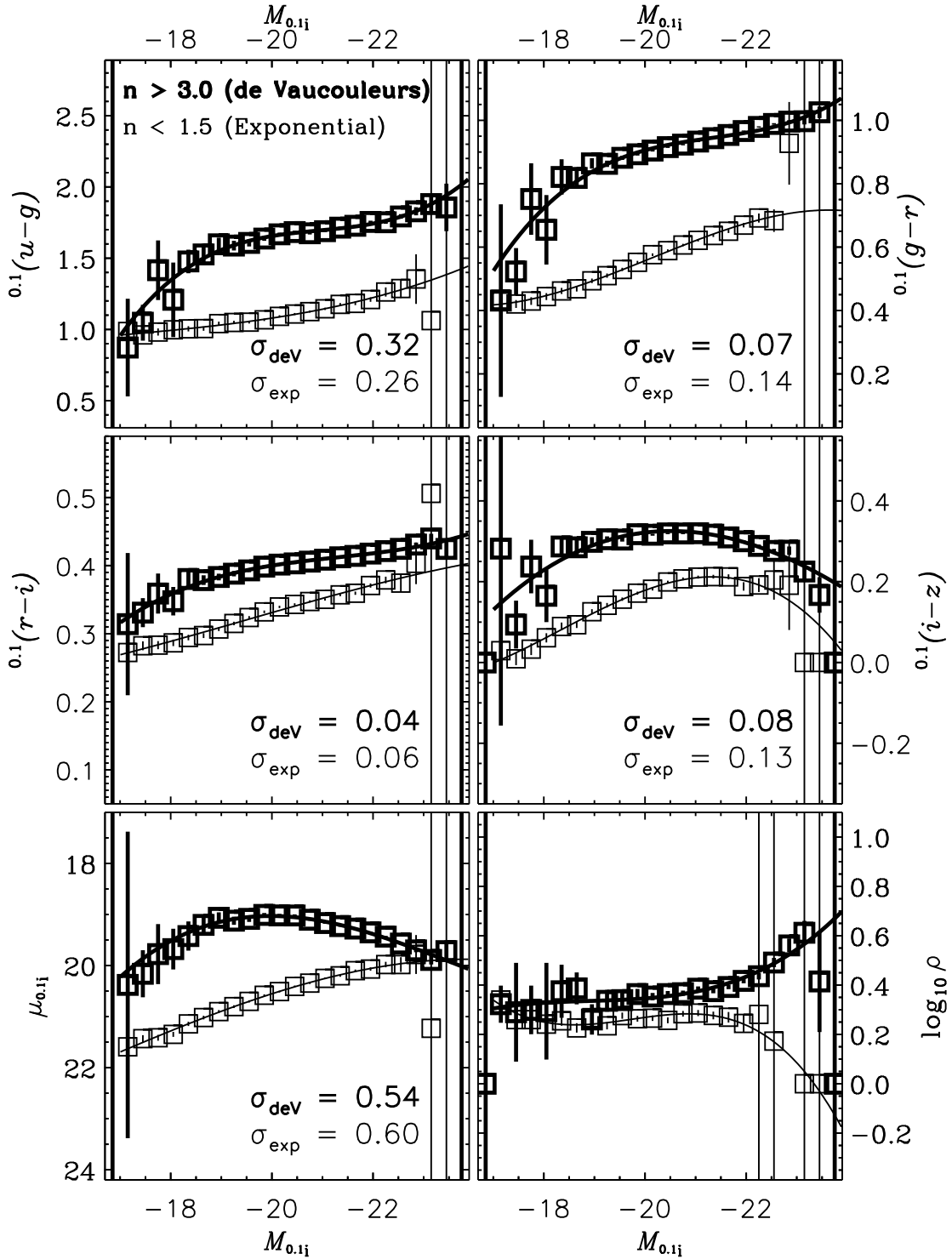


Fig. 14.— Median galaxy properties for concentrated galaxies ($n > 3$; thick lines) and exponential galaxies ($n < 1.5$; thin lines). The measured data points are the boxes, with uncertainties shown as vertical bars. The cubic polynomial fits of the form of Equation 13 are the continuous lines; the parameters of these fits are listed in Table 1. The 1σ deviation around these fits are listed in each panel (and listed in Table 1). The separation between exponential and concentrated galaxies is clear.

Table 1. Fits to Median Galaxy Properties as a Function of Luminosity

Galaxy Type	Property	Units	σ	p_0	p_1	p_2	p_3
Concentrated ($n > 3.0$)	$^{0.1}(u - g)$	mags	0.321	1.697	-0.0338	0.0023	-0.01005
	$^{0.1}(g - r)$	mags	0.068	0.937	-0.0238	-0.0039	-0.00400
	$^{0.1}(r - i)$	mags	0.036	0.410	-0.0082	-0.0007	-0.00077
	$^{0.1}(i - z)$	mags	0.076	0.322	0.0132	-0.0132	-0.00053
	$\mu_{0.4i}$	mags in 1 arcsec ²	0.542	19.131	-0.1866	0.0759	0.00981
	$\log_{10} \rho$	—	0.344	0.373	-0.0413	0.0168	-0.00269
Exponential ($n < 1.5$)	$\log_{10}[r_{i,50}/(1 h^{-1} \text{ kpc})]$	—	0.109	0.305	-0.2370	0.0154	0.00277
	$^{0.1}(u - g)$	mags	0.262	1.142	-0.0712	0.0095	-0.00076
	$^{0.1}(g - r)$	mags	0.143	0.621	-0.0606	-0.0045	0.00175
	$^{0.1}(r - i)$	mags	0.063	0.352	-0.0205	-0.0006	0.00013
	$^{0.1}(i - z)$	mags	0.132	0.210	-0.0139	-0.0194	0.00243
	$\mu_{0.4i}$	mags in 1 arcsec ²	0.600	20.266	0.2545	0.0348	-0.00230
	$\log_{10} \rho$	—	0.371	0.283	0.0080	-0.0298	0.00782
	$\log_{10}[r_{i,50}/(1 h^{-1} \text{ kpc})]$	—	0.123	0.533	-0.1468	0.0061	-0.00030

Note. — Lists fit parameters p_i (see Equation 13 in the text) for galaxy properties as a function of absolute magnitude $M_{0.4i}$, for our exponential and de Vaucouleurs galaxies separately. One can use these relations to predict the galaxy properties given the luminosity, but not vice-versa.